T · H · E
OHIO
STATE
UNIVERSITY

The Effects of Magnetic Nozzle Configurations On Plasma Thrusters

Thomas M. York
Department of Aeronautical and Astronautical Engineering

National Aeronautics and Space Administration
Lewis Research Center
Cleveland, Ohio 44135

Grant No. NAG 3-843
Semi-Annual Progress Report
RF Project 766488/720331

February 1990

AAE Report AARL-P-90-1

SEMI-ANNUAL PROGRESS REPORT
for the period
July 1, 1989 - December 31, 1989

on

THE EFFECTS OF MAGNETIC NOZZLE CONFIGURATIONS ON PLASMA THRUSTERS

Principal Investigator:

Dr. Thomas M. York
Professor and Chairman
Aeronautical and Astronautical
Engineering Department
The Ohio State University
2036 Neil Avenue Mall, 328 Bolz Hall
Columbus, Ohio 43210

Technical Officer:
M.A. Mantenieks
Low Thrust Propulsion Branch
MAIL STOP: 500-219
NASA Lewis Research Center
21000 Brookpark Road
Cleveland, Ohio 44135

RF PROJECT NO.:	MASTER PROJECT:	START DATE:	END DATE:
720331	766488	05 Dec 87	31 Oct 90

SPONSOR:	GRANT/CONTRACT NO.:	SPONSOR ID NO.
Lewis Research Center	NAS 3-843	30030104

Submitted

February 1, 1990

720331.tmy

TABLE OF CONTENTS

ABSTRACT

Plasma thrusters have been operated at power levels from 10kw to 0.1MW. When these devices have had magnetic fields applied to them which form a nozzle configuration for the expanding plasma, they have shown marked increases in exhaust velocity which is in direct proportion to the magnitude of the applied field. Further, recent results have shown that electrode erosion may be influenced by applied magnetic fields. This research effort is directed to the experimental and computational study of the effects of applied magnetic field nozzles in the acceleration of plasma flows. Plasma source devices which eliminate the plasma interaction in normal thrusters are studied as most basic. Normal thruster configurations will be studied without applied fields and with applied magnetic nozzle fields. Unique computational studies will utilize existing codes which accurately include transport processes. Unique diagnostic studies will support the experimental studies to generate new data. Both computation and diagnostics will be combined to indicate the physical mechanisms and transport properties that are operative in order to allow scaling and accurate prediction of thruster performance.

I. INTRODUCTION

The research carried out during the past six months involved a distinct transition from earlier efforts. In this time period, there was a very strong focus on the operation, performance, and diagnostics of a 1/4-scale MPD device. That change of direction was required primarily by programmatic needs. First, a review of all efforts funded under NASA Advanced Propulsion programs was held at NASA Headquarters on October 11, 1989. Second, the progress of research at NASA Lewis on the low power MPD with applied fluids required that we develop our diagnostic studies as rapidly as possible to support that work. Third, with major changes in NASA priorities due to budgeting pressures, there was a need to focus on the primary device that was closest to application.

A brief outline of each of the component efforts will now be presented. Detailed discussion of progress will be reported in subsequent chapters.

1. Experiment

1.1 Plasma Acceleration Studies: Test Facility

Prior to this reporting period, individual simple diagnostics had been employed and, in general, had performed their basic function. Included in these were Rogowski Loop, voltage probes, local magnetic probes, but without the active plasma discharge in the MPD configuration. The transition to gas flow through the MPD anode-cathode configuration produced considerable opportunity for spurious signal generation, including ground loops.

Most basic, however, was the need to provide adequate gas feed into the thruster geometry. This involved a rather extensive effort to develop a pulse generator to provide the fastest pressure rise and most uniform feed pressure for the thruster. These results will be discussed. Comparison of vacuum vessel

background pressures with other "standard" systems is important and will also be described here.

The interaction of circuits involving diagnostics and discharge circuitry produced problems with spurious (noise) signals. A comprehensive evaluation of the ground system was undertaken and corrections affected.

Lastly, there was the development of a switch mechanism which would allow the magnetic nozzle capacitor bank and the thruster discharge capacitor bank to charge to different voltages.

1.2 Operation and Electrical Characteristics of the 1/4-Scale MPD

The generation of acceptable discharge current and voltage parameters for the scaled thruster device did not insure satisfactory performance of the device. The observation of acceptable voltage records, e.g. without high and low frequency oscillations, was found to be related to thruster mass flow rates. Specifically, scaled $\dot{m}$ produce "hashy" records, but enhanced $\dot{m}$ produced smoothly varying voltage records. Similarly, discharge characteristics as indicated by local magnetic probes near the thruster exit were acceptable only with higher $\dot{m}$ values.

1.3 Thruster Diagnostic Studies: Magnetic Field and Impact Pressure

An understanding of the thruster acceleration mechanisms can most basically be determined by studying the acceleration field (i.e. the cause) and the gas momentum (i.e. the effect). These were carried out with local magnetic and pressure probe diagnostics studies. While difficulty was experienced because of the low power level and size of the device, the diagnostics difficulties were overcome and truly unique data histories were recovered.

1.4 Thruster Diagnostic Studies: Applied Magnetic Nozzle Effects

The application of a simple magnetic nozzle configuration was found to produce effects in all the data gathered: current, voltage, local magnetic field, and local impact pressure. Even at low power and relatively low ionization, the effects were found to be considerable. While these studies are still underway, this report will provide a review of the up-to-date results.

1.5 Diagnostic Development: Thomson Scattering

Considerable effort was devoted to achieving an operational Thomson Scattering system for N_e, T_e. While much progress was made, work had to be terminated in early November due to a lack of funds. This diagnostic is important to provide N_e which is combined with data from impact pressure, but also to provide direct measurement of electron drift velocity. We will continue this development effort as soon as possible.

1.6 Diagnostic Development: Spectroscopy

Since the experimental studies are most critical, and as knowledge of the experiment can provide a firm base for theoretical studies, a Graduate Associate who had been developing computational models, began a basic study of spectroscopic techniques, the application of the (¼ m monochromatic) spectroscopic system available to us, and the development of a system to conduct spectroscopic studies.

2. Theory

2.1 Inclusion of Hall Effect Terms in Magnetic Nozzle Model

Previous studies had concentrated on the development of a computational model to allow comparison of plasma flow within applied axially expanding magnetic fluid lines. Specifically, there were no applied electric fields which could be capable to generating multiple complex interactions. As a first step at including Hall effect, (cross field) terms due to (VxB_r) interactions have been examined and included. Further work is needed, but this initial effort will set the direction for further studies.

3. Diagnostic Development Under Complementary Research Grants

During this time period, work was begun to design and develop a multi-beam interferometer system using a CW CO_2 laser system under AFOSR sponsorship. The application of this new diagnostic is intended to be the 1/4-scale thruster and magnetic nozzle flows of interest to NASA. The system has been designed, components procured and testing and assembly are now underway. A test-bed experiment, independent of the thruster, will be set up to establish proof of principle.

II. EXPERIMENTAL STUDIES OF ¼-SCALE MPD THRUSTER ACCELERATION

Zakrzwski and Soulas

1. Test Facility and Experimental Apparatus

1.1 Introduction

In order to operate the ¼-scale MPD thruster and to successfully employ simple diagnostics, alterations to the thruster itself and to the test facility had to be made. The most important change to the experimental apparatus was in the development of a gas feed system for the thruster. This effort included the fabrication of a pulse generating circuit to operate a Skinner Solenoidal valve (Model V520B2100, Honeywell Skinner Valve Division, New Bruton, CT) that controlled the gas feed to the thruster. The test facility electrical circuits were altered in order to obtain reliable measurements that were free of external noise. These changes were made after a comprehensive evaluation of the grounding and shielding systems was performed. Also included in the changes to the test facility was the addition of a switching system which allows the thruster bank and the magnetic field bank to be charged to different voltage levels. Voltage on both banks could be monitored.

1.2 Gas Feed System

The gas feed system for the ¼-scale MPD thruster was designed, within available resources, to reliably provide a uniform gas flow into the thruster electrical discharge chamber. The transient time before achieving a steady-state flow was made as short as possible in order to minimize the back pressure build up in the vacuum chamber. The major components of the gas feed system are shown in Figure 1. They include the thruster plenum, the reserve plenum, and the Skinner valve connecting the two plenums. The mass flow rate produced by the gas

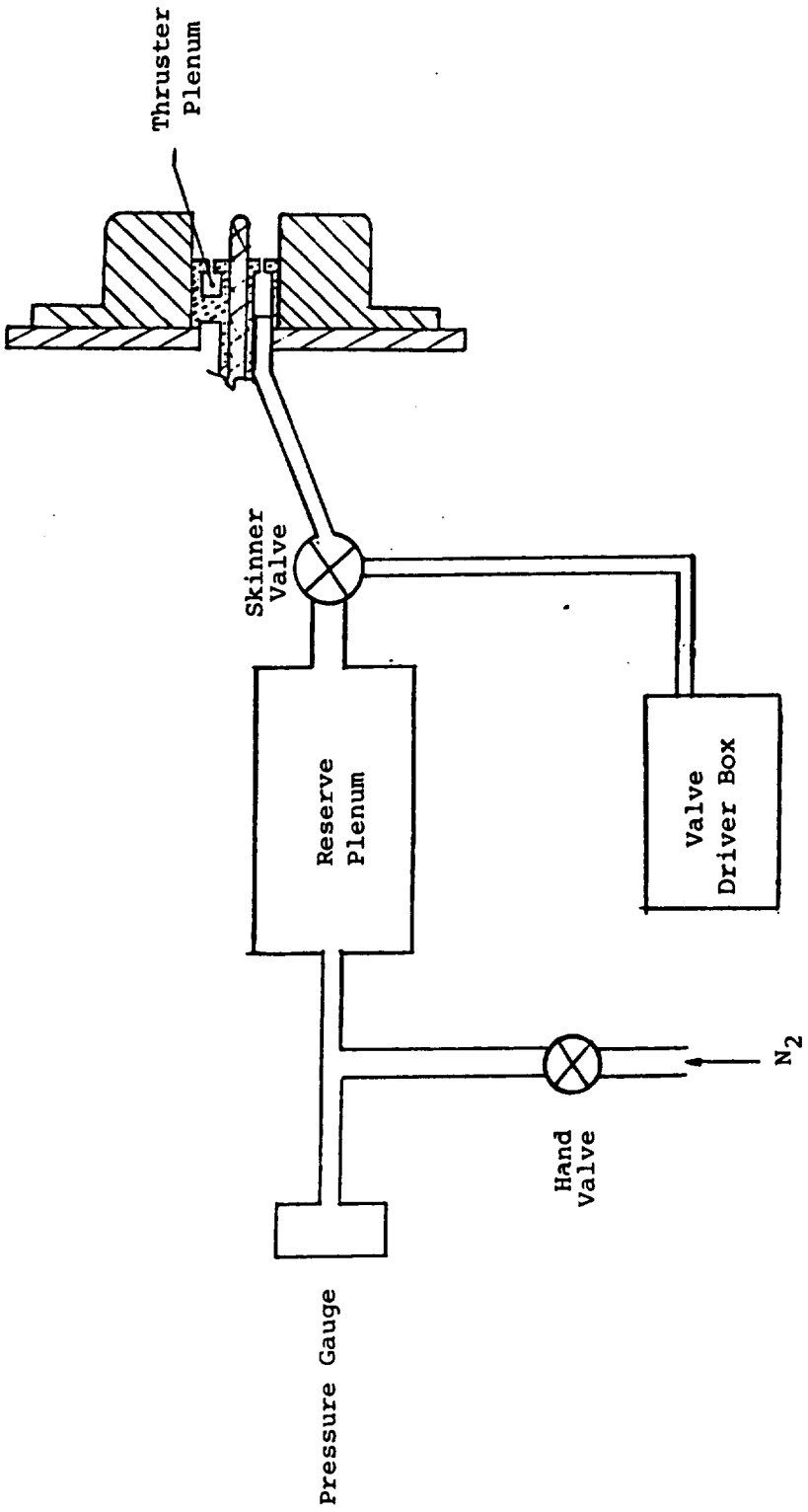

Figure 1: Gas Feed System Components

feed system is set by fixing the initial pressure in the reserve plenum. This pressure is monitored by a Baratron type 22BA-01000AB pressure transducer (MKS-Instruments, Inc., Burlington, MA). Because of the small volume of the thruster plenum compared to the reserve plenum (a ratio of nearly 1000:1), the pressure in the thruster plenum is brought to the initial pressure in the reserve plenum once steady state flow is achieved. Knowing the pressure in the thruster plenum, the area of the gas ports in the back plate of the discharge chamber, and with the assumption that the flow is choked at the gas ports, the mass flow rate can be determined.

The main component of the gas feed system is a Skinner valve which delivers propellant to the thruster. It is the opening time of this valve that determines how high the back pressures in the vacuum chamber will be during the operation of the thruster. To open this valve as quickly as possible, a special circuit was designed to "overdrive" the solenoid coil in the valve, which is normally rated for 24 V at 60 hz. The final version of this circuit is a modification of the valve driver circuit presented in the previous progress report.[1] The basic operating principle remains the same. The charge stored on a 200 μF capacitor array, normally at 50 V, is impressed on the valve by opening an SCR switch. The present configuration uses a relay switch to short the coil and thus close the valve. This relay switch replaces an SCR switch used in the previous design. The relay switch is actually triggered before the SCR is activated because of the inherent delay in the relay. Timing of the circuit is controlled by a series of cascade timers.

The time needed to reach steady state flow in the thruster was measured with the test cell described in the previous progress report. This test cell mimics the thruster plenum and used a quartz pressure transducer (Model 606A,

Kisler Instruments Corporation, Clarence, NY) to measure the pressure history in the thruster plenum. The minimum rise time for the pressure in the thruster plenum was found to be 5 msec. A sample of the test results is shown in Figure 2. This record is for an initial reserve plenum pressure of 150 Torr. The initial pressure of the plenum was varied from 100 to 760 Torr with no noticeable change in the rise time. The rise time for the pressure appeared to be limited by the length of tubing connecting the Skinner valve to the thruster plenum. Increasing the voltage pulse up to 150 V did not change the rise time. The length of the tubing was large, i.e. 8 cm, relative to its inner diameter, 0.4 cm. This length was necessary in order to prevent arcing from the discharge chamber to the valve. The length was calculated assuming a pressure of 150 Torr in the thruster plenum with a maximum voltage of 13 kV (see Reference (2)).

The back pressure in the vacuum chamber was estimated with the known behavior of the mass flow rate and the volume of the vacuum chamber. The mass flow rate at which the thruster was operated for all of the data presented in this report was 0.135 gm/sec. This mass flow rate was chosen for reasons to be discussed in the following section. This mass flow rate corresponds to an estimated back pressure of 7 mTorr at the time of firing. These parameters are listed in Table 1 with comparisons between the ¼-scale thruster and those reported from full-scale devices. The numbers shown for the Princeton full-scale thruster have been calculated from the information given in Reference (3). While back pressure effects on thruster performance have been widely reported, some studies have indicated that this level of back pressure may have only slight effects on the self-field performance.[4]

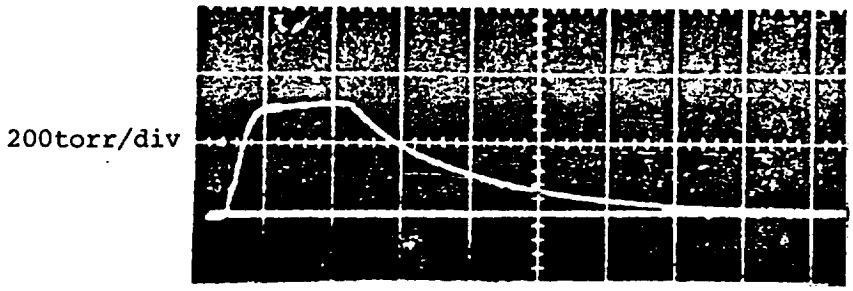

Figure 2: Pressure History of Thruster Plenum

Table 1: Comparison of Operating Condition for 1/4-Scale and Full-Scale MPD Thrusters

	Initial Pressure (torr)	Scaled $\dot{m}$ (gm/sec)	Pressure at Ignition (torr)	Pressure at End of Discharge (torr)
1/4-Scale	$> 1x10^{-3}$	0.135	$7.0x10^{-3}$	$7.7x10^{-3}$
Full-Scale (Princeton)	$> 1x10^{-5}$	2.16	$3.24x10^{-3}$	$4.1x10^{-3}$

1.3 Test Facility Modifications

Modifications were made to the test facility in order to obtain reliable diagnostic measurements that are free of external noise. In order to avoid ground loop pick-up from the diagnostics, new grounding plates were run from the screen room to the thruster and backplate (opposite the thruster) ends of the vacuum chamber, and all coaxial cables from the diagnostics were routed along these plates. The connection to ground was made on the ground side of the thruster. The grounding plates were made of 20 gauge copper and aluminum sheet metal, with a minimum width of 12 in. These grounding plates proved useful in obtaining reliable voltage probe measurements since this diagnostic was found to be sensitive to ground loops. These grounding plates were also important in establishing a common ground for the screen room and the experiment.

It was determined that for the sake of safety and the prevention of ground loops, there should only be a single path to a ground which would be separate from building power or other grounds. Steps were taken to achieve this goal. First, mylar was used to insulate the experiment from contact with any conductor that might lead to a separate ground. Second, since the oscilloscope was now grounded to the experiment, a 1000 watt isolation transformer (Magnetek-Triad, Huntington, IN) was used to isolate the oscilloscope from the power line. Third,

in order to establish a ground separate from the building, an 8 ft., 0.75 in. diameter, copper plated grounding rod was inserted into the ground 3 ft. from the building. This rod became the experiment's single path to ground.

Once these modifications were made, the effectiveness of the grounded screen room in shielding the oscilloscope from noise was tested. It was determined that reliable measurements could be taken from signals as small as 5 mV. However, it was found that within the screen room, diagnostic signals which were large in magnitude, particularly the signals of the Rogowski loops, did interfere with diagnostic signals in the millivolt range. Therefore, two separate screen rooms were used, one for the Rogowski loop and the other for the other more sensitive diagnostic(s).

1.4 Capacitor Bank Switch

A simple mechanical switch was fabricated to allow the capacitor banks of the thruster and magnetic field to be charged to different voltages. The charge line from the power supply was connected to each individual bank through these switches. This allowed the controller to charge both banks to a certain voltage, disconnect one of the banks from the power supply, and continue to charge the other bank to a higher voltage. A voltage meter is used to monitor the voltage of the disconnected capacitor bank.

2. Operation and Characteristics of the ¼-Scale MPD

2.1 Introduction

The operating characteristics of the ¼-scale MPD were first examined by measuring the electrical characteristics. These electrical characteristics include the current-voltage trends across the anode and cathode, and the distri-

bution of current in the exhaust plume. Results from initial current-voltage measurements led to an increase over ideal scaled values of the mass flow rate for thruster operation. Results from local magnetic field probes used to map the enclosed current in the exhaust plume, led to a change in the thruster mass injection scheme. Both of these changes improved the operating characteristics of the thruster and produced a stable arc.

2.2 Current-Voltage Measurements

Measuring the current-voltage characteristics gave the first insight into the operating condition of the thruster. The voltage was measured with a Tektronix P6105 1000x Voltage Probe (Tektronix, Portland, OR) which was attached to the copper feed plate to the cathode. The current was measured with a Rogowski loop which was connected to a passive integrator both of which are described in a previous progress report. Both current and voltage signals were measured on a Tektronix 551 oscilloscope (Textronic Inc., Portland, OR) when the thruster was operated in the self-field mode. When the thruster was operated with an applied magnetic field, the current signal was monitored on a separate oscilloscope, a Tektronix 555 (Tektronix, Inc., Portland, OR) that had its own isolated screen room. This was necessary in order to eliminate noise from being brought in from the Rogowski loop coaxial cable and being transferred to the voltage probe signal.

The first current-voltage characteristic for the thruster was measured for a mass flow rate of 0.034 gm/sec of nitrogen. The voltage traces indicated that the thruster was operating in an erratic fashion because of the high frequency oscillations that appeared as hash (i.e. oscillations) on the trace. An example of this is shown in Figure 3. It was concluded from this that the amount of gas

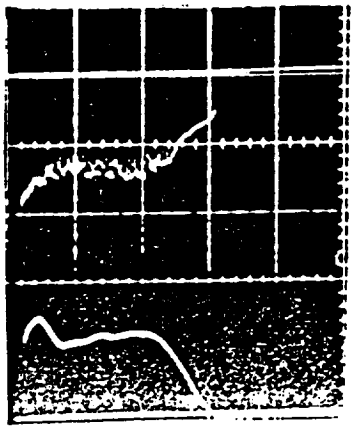

Figure 3: Current and Voltage Measurement at $\dot{m}$=0.034gm/sec and I=1.15kA

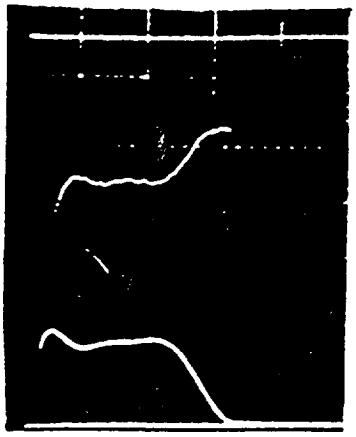

Figure 4: Current and Voltage Measurement at $\dot{m}$=0.068gm/sec and I=1.15kA

in the discharge chamber may not be sufficient for a stable discharge. Increasing the mass flow rate to 0.068 gm/sec of nitrogen significantly improved the voltage behavior. The voltage record was smoother and followed the current wave form more closely. An example of this is shown in Figure 4. While the voltage records were greatly improved for a mass flow rate of 0.068 gm/sec, the voltage trace would still occasionally have some high frequency oscillations when running at the standard current level of 1.15 kA.

2.3 Local Magnetic Field Probe Measurements

After the indicated operation at a higher mass flow rate, the characteristics of the electrical thruster discharge was further investigated with local magnetic field probes. These probes, which will be described in the next section, were placed in the exhaust plume in order to measure the azimuthal self-induced magnetic field so as to determine the current distribution in the exhaust plume. Initial results showed large oscillations in the magnetic field during the steady state portion of the current trace. The nature of the oscillations varied from shot to shot with the probe at the same position. It is thought that these oscillations were from an unstable arc that may have been rotating, however, there were no means readily available to determine this. Further, increasing the mass flow rate by a factor of 2.5 did not improve the magnetic field signals. Accordingly, tests were then run using a combination of gas pre-fill in the vacuum chamber and mass injection from the back plate of the thruster. Reasonable magnetic field signals, i.e. fields that followed the current wave form, were obtained at pre-fill pressures of 120 millitorr and with gas being injected at, or above, 0.068 gm/sec.

It was concluded from the above test results that the cathode was mass starved because of an uneven distribution of gas in the discharge chamber. This, in turn, was concluded to lead to the type of erratic magnetic field signals that were being measured. To overcome this problem, eight additional gas ports (0.36 mm in diameter) were added around the base of the cathode. These holes were approximately 1.5 mm from the cathode surface and are shown with the original eight gas feed holes in Figure 5. After these new ports were added, additional tests were run to determine what mass flow rates, if any, would produce reasonable magnetic field signals. A mass flow rate of 0.135 gm/sec was the lowest rate that produced smooth and predictable magnetic field records. This mass flow rate corresponded to a reserve plenum pressure of 295 Torr. Lower mass flow rates induced magnetic field signals which had greater oscillations. This can be seen in Figure 6 where a mass flow rate of 0.045 gm/sec is compared to a mass flow rate of 0.135 gm/sec. Since higher mass flow rates increase the back pressure in the vacuum chamber at the time of firing the thruster, it was decided to run all the tests in this report at the 0.135 gm/sec mass flow rate. This ¼-scale mass flow rate corresponds to a full scale mass flow rate of 2.16 gm/sec.

3. Thruster Diagnostic Studies: Magnetic Field and Impact Pressure

3.1 Introduction

The two primary diagnostics used to examine the exhaust field of the ¼-scale MPD thruster were magnetic field probes and piezoelectric pressure probes. The magnetic field probes were used to measure magnetic field strengths and current densities within the exhaust plume; the pressure probe was used to measure local impact pressures of the exhaust plume. The information obtained from these probes was then used to examine the operation of the ¼-scale MPD. Difficulties

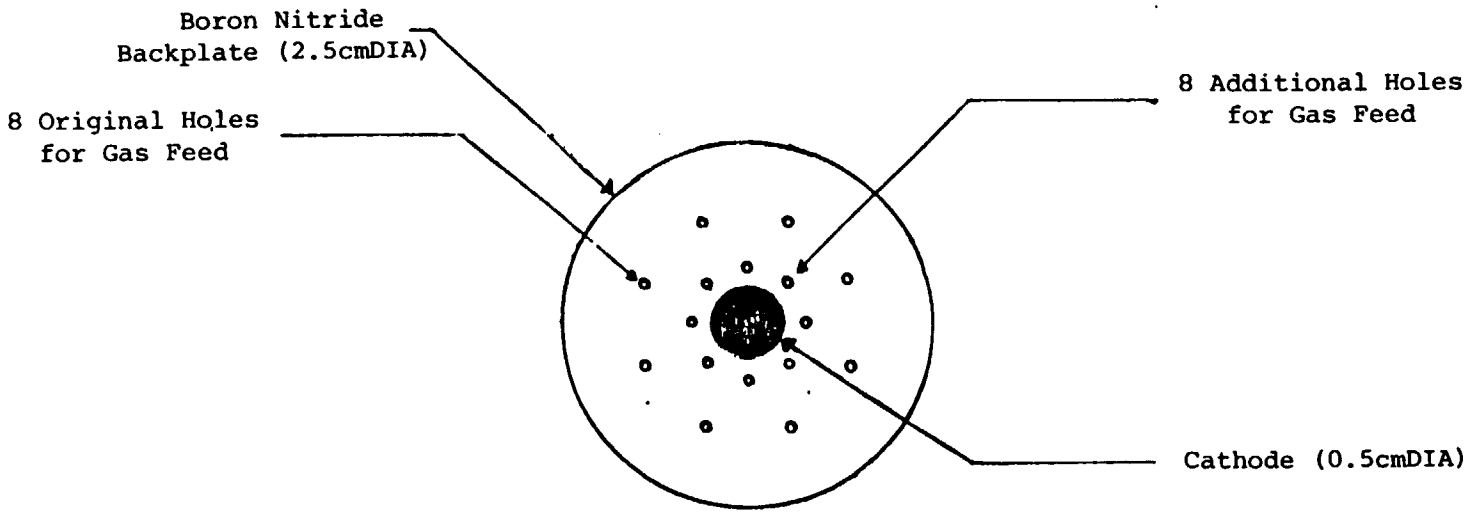

Figure 5: ¼-Scale MPD Backplate

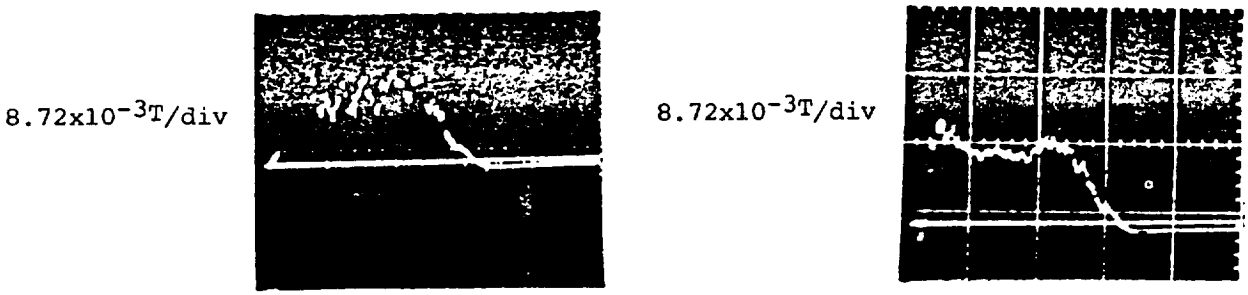

100μsec/div
(a) $\dot{m}$=0.045gm/sec

100μsec/div
(b) $\dot{m}$=0.135gm/sec

Figure 6: Azimuthal, Self-Induced Magnetic Field at r=0.6cm and z=1.0cm

were encountered in designing these probes to overcome the extreme environment of the exhaust plume and the electrical noise effects of the discharge.

3.2 Magnetic Field Probes

Magnetic field probes using solenoidal coiled wire to measure the rate of change of magnetic flux within the coil were constructed and operated in the experimental discharge. Several different sizes and types were constructed which produced adequate results. To achieve a readable signal, an active integrator was used along with a 50 Ω terminator in the signal cable.

The magnetic field probe used to determine discharge stability had a sensor that was made of 40 gauge wire (Belden, Geneva, IL) wrapped 330 times around a 6 mm diameter pyrex tube that was 7 mm wide. This sensor was cast in epoxy and then epoxied perpendicular to a 7 mm diameter pyrex tube which was over 120 cm long. A type 9234 coaxial cable (Belden, Geneva, IL) was connected to the sensor and run through the 120 cm long tube with care taken to shield the connection. The probe was calibrated by placing the sensor in the center of a 9 cm long, 5.5 cm diameter coil of 1/8 in copper wire which was attached to the thruster capacitor bank. The calibration for this probe was found to be 8.72x10 Tesla/V.

A second, smaller probe was constructed for use in mapping the current contours in the exhaust plume. This probe was constructed in a similar manner to the one described above. The sensor consists of 40 wraps of 40 gauge wire around a 1 mm diameter center; this was enclosed within a 3 mm inner diameter, 5 mm outer diameter pyrex tube. This probe has the addition of 0.5 mm thick copper tubing around the coaxial cable that is inside the 120 cm pyrex tube.

An active integrator was built to integrate the signal from the magnetic field probes. This was necessary since a passive integrator, with a time con-

stant of 8.75 msec, produced too small a signal in relationship to the noise being picked up on the oscilloscope. The active integrator is based on a simple design found in Reference (5). This design uses a type 741 operational amplifier with an 18 V power supply. The active integrator improved the signal that could be measured using the passive integrator by a factor of 20.

When the magnetic field probes were used, a high frequency oscillation that dominated the total signal being generated by the magnetic field probe was found. This oscillation was caused by intermittent cable "ringing." In addition to the 50 Ω terminator, a passive filter with a time constant of 5.4 μsec was used after the active integrator when readings were taken at or below the 10 millivolt/div setting on the oscilloscope. This was necessary in order to eliminate high frequency "hash" produced by the active integrator at this low operating level.

A sample of the magnetic field traces is shown in Figure 7. Figure 7a shows the self-field without the applied field and Figure 7b shows the self-field with the applied field. For each position, a trace was also taken with the magnetic field coil only being fired. The azimuthal magnetic field, measured solely due to the applied field, was often significant. However, it was only slightly noticeable in the example in Figure 7. Because magnetic fields follow the principle of superposition, the self-field in the applied field shot is taken to be the difference between the trace with the magnetic field and the trace with both the thruster and magnetic field in operation. It is this difference that is used to calculate the enclosed current.

3.3 Pressure Probe

The pressure probe used was a probe specially designed for testing MPD thrusters. As stated in the previous progress report, the probe had to be

0.123 T/div

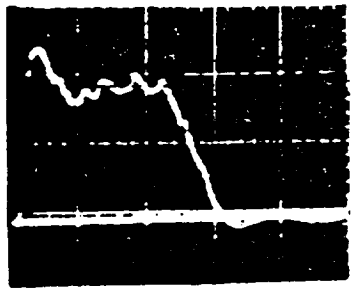

100μsec/div

(a) Thruster Only

0.123 T/div

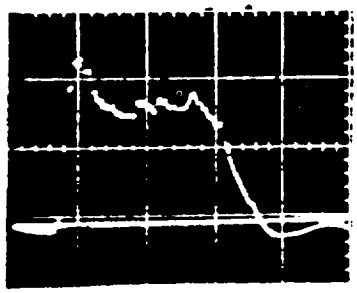

100μsec/div

(b) Thruster with Applied Magnetic Field

Figure 7: Azimuthal Magnetic Field at r=0.6cm, z=0.8cm, I=2.3kA, and $\dot{m}$=0.135gm/sec

designed to overcome the electrical contact with the plasma, the electrical noise effects of the discharge, and the extreme thermal environment of the exhaust plume in order to obtain reliable measurements.

The pressure probe used was a unique design different from the commercial probe that was discussed in the previous progress report. That commercial probe produced signals with high frequency oscillations when tested in a shock tube, and therefore, its use had to be discontinued. The new unique design pressure probe utilizes a piezoelectric ceramic element supported on a structure of backing rod in an insulated housing, as shown in Figure 8. This unit was epoxied into a quartz tube with the sensing surface tightly bonded to the front, which has a flat fused end.[6] The quartz tube provided insulation from plasma contact while allowing stress to be transmitted through the quartz to the sensor. The output of the probe was matched with an amplifier (x10) and follower of unique design. The probe was calibrated using a simple shock tube. A calibration constant of 1.04 V/psi was obtained. The probe was rigidly mounted on a back plate opposite the thruster. Since this requires the tubing of the probe to be at least 93 cm long, a pyrex tube, 1.27 cm outer diameter, was epoxied to the back of the quartz tube in order to extend the length of the probe.

Modifications were made on the experimental set-up and the pressure probe in order to obtain reliable measurements. In order to avoid ground loops, the amplifier-follower circuitry and the coaxial cable were placed on grounding plates which run from the back plate to the screen room and oscilloscope. In order to shield the pressure probe from interference due to the magnetic nozzle field, a ¼ in. soft copper tube was placed within the pyrex and quartz tubes, running from the piezoelectric housing unit to the end of the pyrex tube and housing the coaxial cable within. This is shown in Figure 8. Although this does

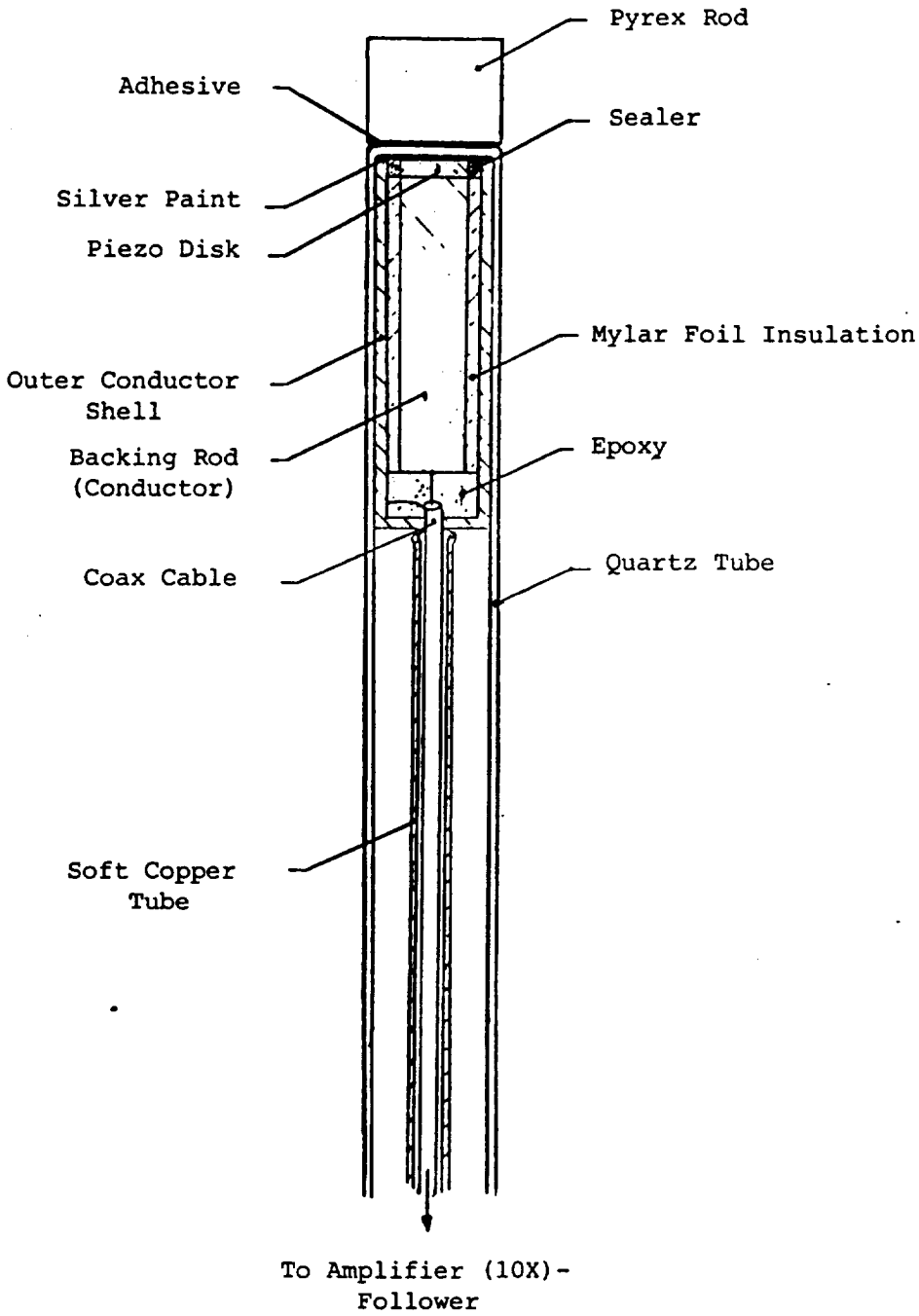

Figure 8: Cross-Section of Pressure Probe

not completely eliminate the effects of the nozzle magnetic fields, it does provide a quiescent period in which reliable pressure measurements from the thruster can be taken.

During the testing of the pressure probe, it was determined that additional modifications would have to be made on the experimental set-up and the pressure probe. Since the pressure probe and the Skinner valve of the ¼-scale MPD thruster were both rigidly mounted onto the vacuum chamber, a high amplitude, low frequency oscillating signal caused by the vibration from the Skinner valve opening was superimposed on all pressure signals. A damping-sealer (Macklanburg-Duncan, Oklahoma City, OK) was place between the Skinner valve and its mounting plate in order to dampen this vibration. Furthermore, because of the rigid manner in which the pressure probe was mounted onto the back plate, a high frequency oscillating signal, caused by the shock from the blast wave of the discharge striking the pressure probe, was superimposed onto all pressure signals.[7] To eliminate shock and thermal effects, a pyrex rod 1.1 cm long, was fixed to the pressure probe with two layers of tape (Scotch 3M Brand, St. Paul, MN) which served to damp the initial shock of the blast wave while allowing the subsequent pressure history to be accurately measured. Figure 9 shows an example of these results. The pyrex rod further acts as a thermal insulation, guarding the probe from thermal stresses caused by the plasma heating.

Typical pressure probe measurements are shown in Figure 9. These are pressure measurements of the thruster discharge, magnetic nozzle interference, and thruster discharge with a magnetic nozzle. These measurements were taken at cm from the face of the ¼-scale MPD thruster, at a radius of 5 cm.

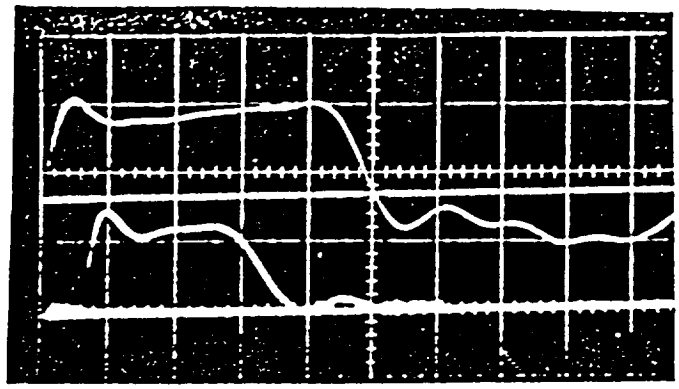

Thruster and Magnetic Field Coil Currents

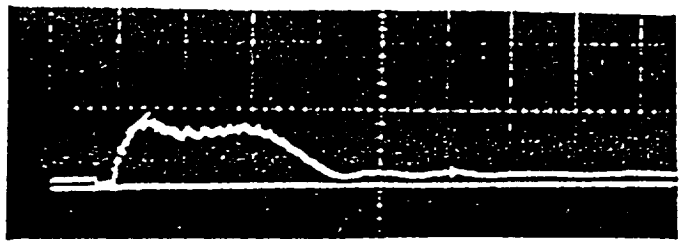

Pressure Probe Response with Self-Field Thruster

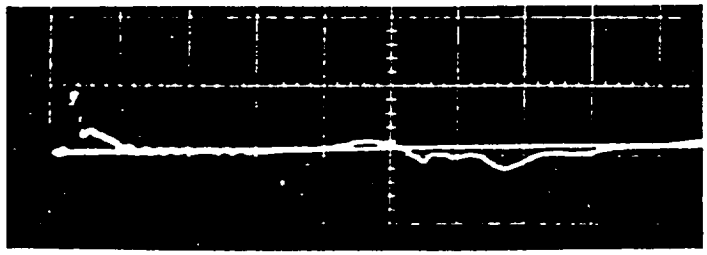

Pressure Probe Response to Applied B Field (no thruster)

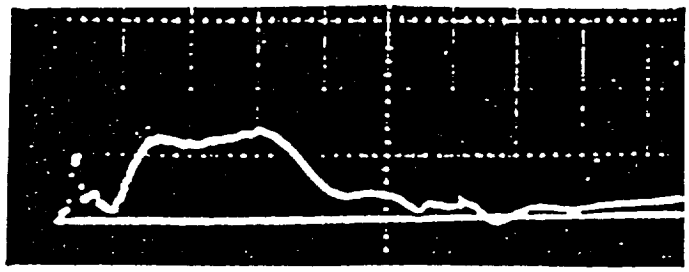

Thruster with B=1KG Applied Field

100μs/DIV
R=0 , z=5cm

Figure 9: Typical Pressure Measurements for ¼-Scale MPD at r=0cm and z=5cm

4. Applied Magnetic Nozzle Effects

4.1 Introduction

The application of an external magnetic field on the 1/4-scale MPD was found to produce significant effects on all of the data measured to date. This included current-voltage measurements, magnetic profiles in the exhaust plume, and impact pressure profiles. Data have been taken for the self-field case and for the case of an applied magnetic field measuring approximately 1200G on the axes of the magnetic field coil. The data were taken at mass flow rates of 0.135 g/sec of N_2 at thruster current levels of both 1.15 and 2.3 kA. The effect of the applied field was similar for both current levels.

The applied field of 1200G was created by charging the magnetic field coil bank to 13 kV. A mapping of this field, with the 1/4-scale thruster in place, was taken with axial and radial local magnetic field probes. A listing of the measured magnetic field values taken at axial positions between 1 and 20 cm from the face of the thruster and at radial positions between 0 and 6 cm is shown in Table 2. These data were used to obtain the magnetic flux lines shown in Figure 10. These lines were created by interpolating the tabular data. It can be seen from the figure that the axis of the flux lines still occurs at the axis of the coil even though the 1/4-scale thruster causes the flux lines to be deflected up for the field near the thruster.

4.2 Current-Voltage Measurements

Current-voltage characteristics for the 1/4-scale thruster were measured with the probes described earlier. The range of currents was obtained by varying the bank voltage from 5 kV to 13 kV, with measurements being taken at 0.5 kV intervals. The spark gap switches for the thruster's PFN had to be set at one

Table 2: Measured Local Applied Magnetic Field Values

Axial (cm) Position	Radial (cm)	1.0 B (G)		2.0 B (G)		3.0 B (G)		5.0 B (G)	
	Position	Axial	Radial	Axial	Radial	Axial	Radial	Axial	Radial
	0.0	90.5	---	861	---	1050	---	1270	---
	1.0	596	-98	969	18.5	1130	97.5	1160	177
	2.0	718	-327	939	-111	1180	61.7	1250	253
	4.0	1578	-407	1407	-185	1460	55.5	1330	296
	6.0	1770	-123	1870	-154	1810	93.8	1240	439

Axial (cm) Position	Radial (cm)	9.0 B (G)		14 B (G)		20 B (G)	
	Position	Axial	Radial	Axial	Radial	Axial	Radial
	0.0	904	---	445	---	195	---
	1.0	869	173	431	112	161	64.1
	2.0	933	313	430	226	158	115
	4.0	847	352	431	191	141	123
	6.0	761	612	316	359	121	163

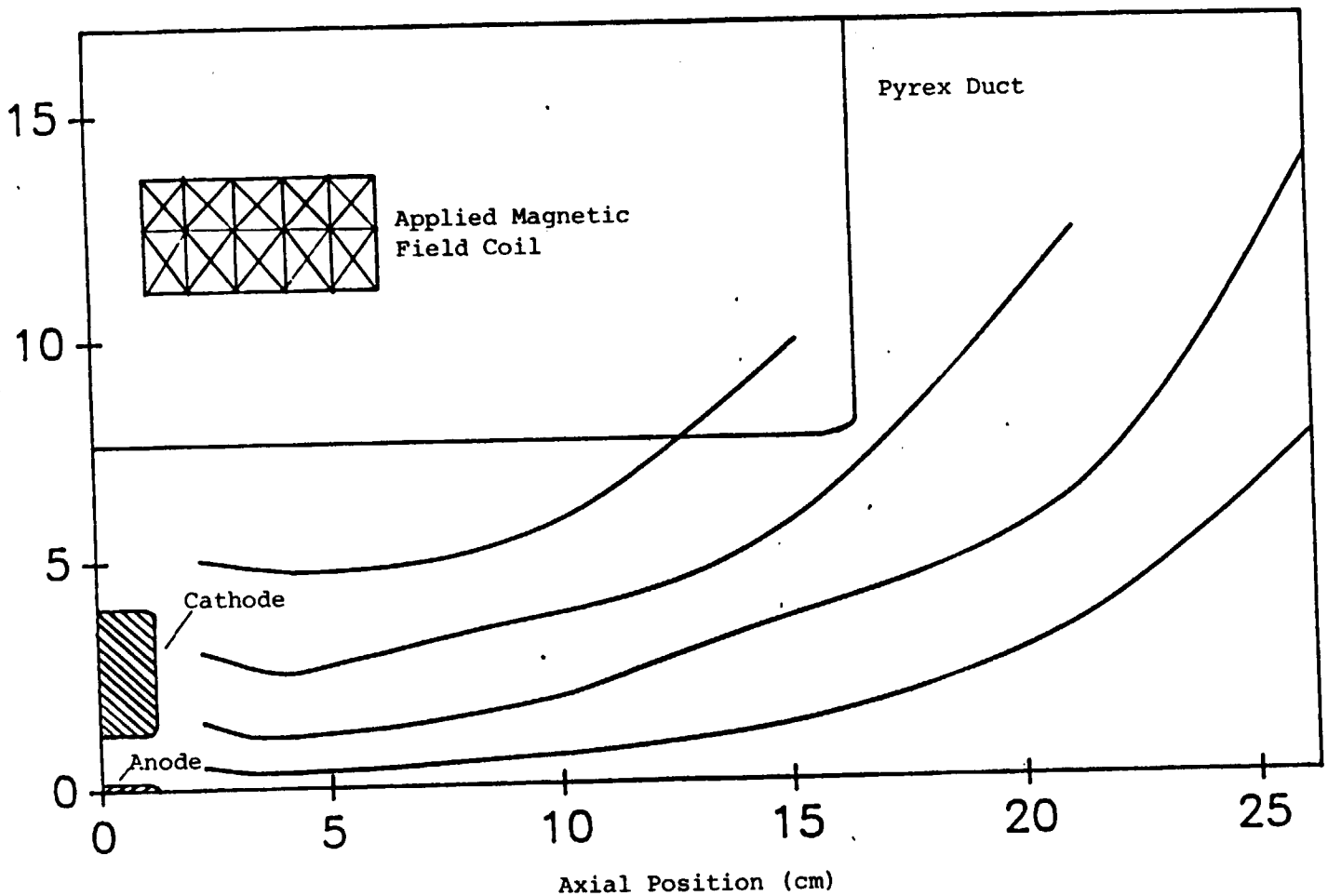

Figure 10: Magnetic Flux Lines for ¼-Scale MPD Tests

position for current levels between 0.8 kA and 1.5 kA, and at a different position for currents between 1.5 kA and 2.3 kA. The current-voltage characteristics for the 1/4-scale thruster as shown in Figure 11.

The current-voltage characteristics indicate the basic operating condition of the thruster. Most fundamentally, the power level at which the thruster operated can be determined for P=IV. At the 1.15 kA level the thruster operated at 55 kW without the applied field and at 59 kW with the applied field. At the 2.3 kA level the thruster operates at 150 kW for both cases. The difference in power levels at the 1.15 kA level is, of course, due to the difference in voltages. The difference in voltages between the two operating conditions is most noticeable when the linear regression for each condition is extended to the zero current level. This extrapolation of the data allows the electrode fall voltage to be estimated. From the figure it can be seen that the fall voltage for the applied magnetic field case is 15 V higher than the fall voltage for the self-field case. The increase in voltage due to the applied magnetic field is anticipated due to the decrease in the conductivity of the plasma as the charge particles try to move against a transverse magnetic field. While back emf may be slightly higher for the applied field case because of increase in velocities, this effect is minimal. Estimates of the back emf, based on averaged velocities obtain from pressure probe data, show that for the self-field case the back emf may contribute 3 V while for the applied-field the back emf may contribute 5 V.

4.3 Current Profiles in the Plume

Enclosed current contours were mapped by measuring the azimuthal magnetic field with local magnetic field probes. The measured magnetic field values were used in the relationship,

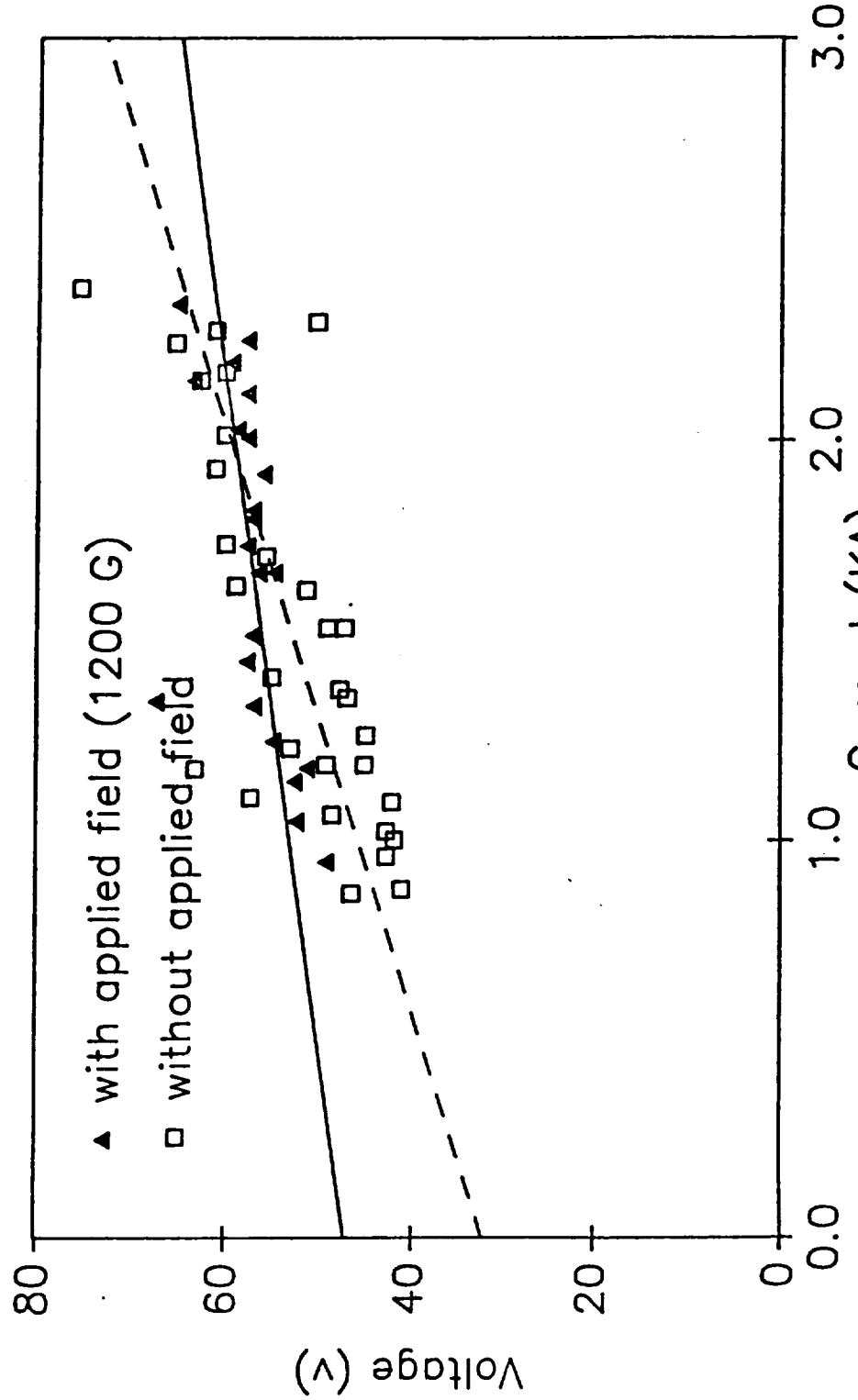

Figure 11: Current-Voltage Characteristics of the ½-Scale MPD

$$I_{en}(r,z) = \frac{2\pi r}{\mu_o} B_\theta(r,z)$$

to find the current enclosed in a given radius at a particular location. The azimuthal field was measured at 6 different radial locations and at axial intervals of typically 0.5 cm. Although data were collected for the thruster operating at 1.15 kA, this data was not reliable enough, due to low signal levels, to be presented. The azimuthal magnetic field data for the thruster operating at 2.3 kA with and without an applied magnetic field is shown in Figure 12 and Figure 13, respectively. The negative signs indicate that the magnetic field reversed direction.

Enclosed current profiles derived from these magnetic field data for the self-field and applied field cases can be seen in Figure 14 and Figure 15, respectively. The profiles were obtained by first finding the enclosed current at the measured magnetic field locations and then interpolating between these points to find lines of constant current. The solid lines in the figures indicate the region between interpolated points, while the dashed lines are extrapolations.

Although the resolution of the mapping is limited by the small probe area involved and the small signal levels, the effect of the applied magnetic field on the current patterns can clearly be seen. For the self-field case 10 % of the current is carried down stream as far as 2.5 times the cathode radius from the backplate. In contrast, for the applied field case 10% of the current is only carried down stream as far as 1.5 times the cathode radius. Overall, it can be seen that the applied magnetic field tends to push the current back inside the discharge chamber. This effect may be related to the confinement of the plasma

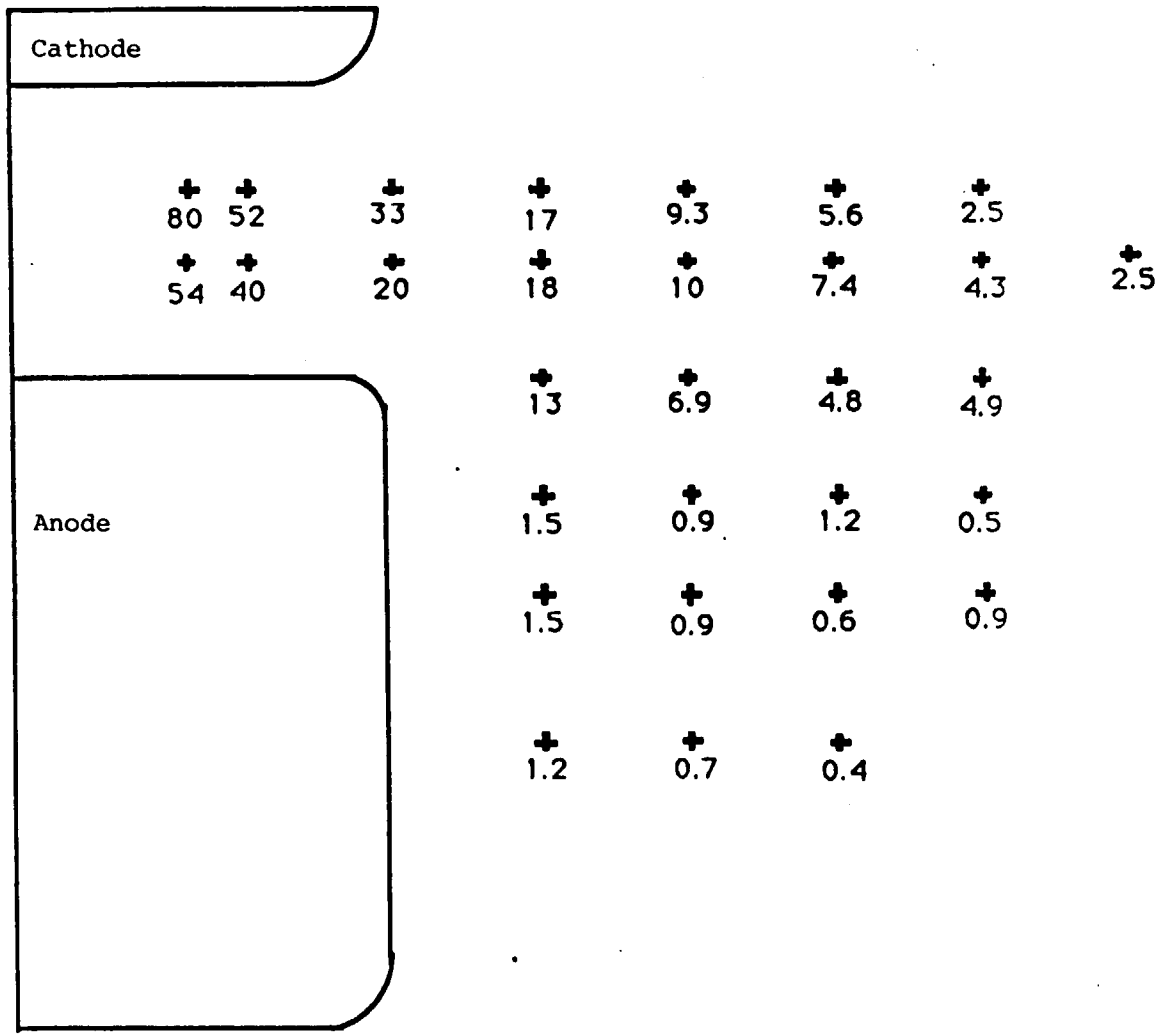

Figure 12: Azimuthal Magnetic Field Data Without Applied Magnetic Field and (I=2.3kA)

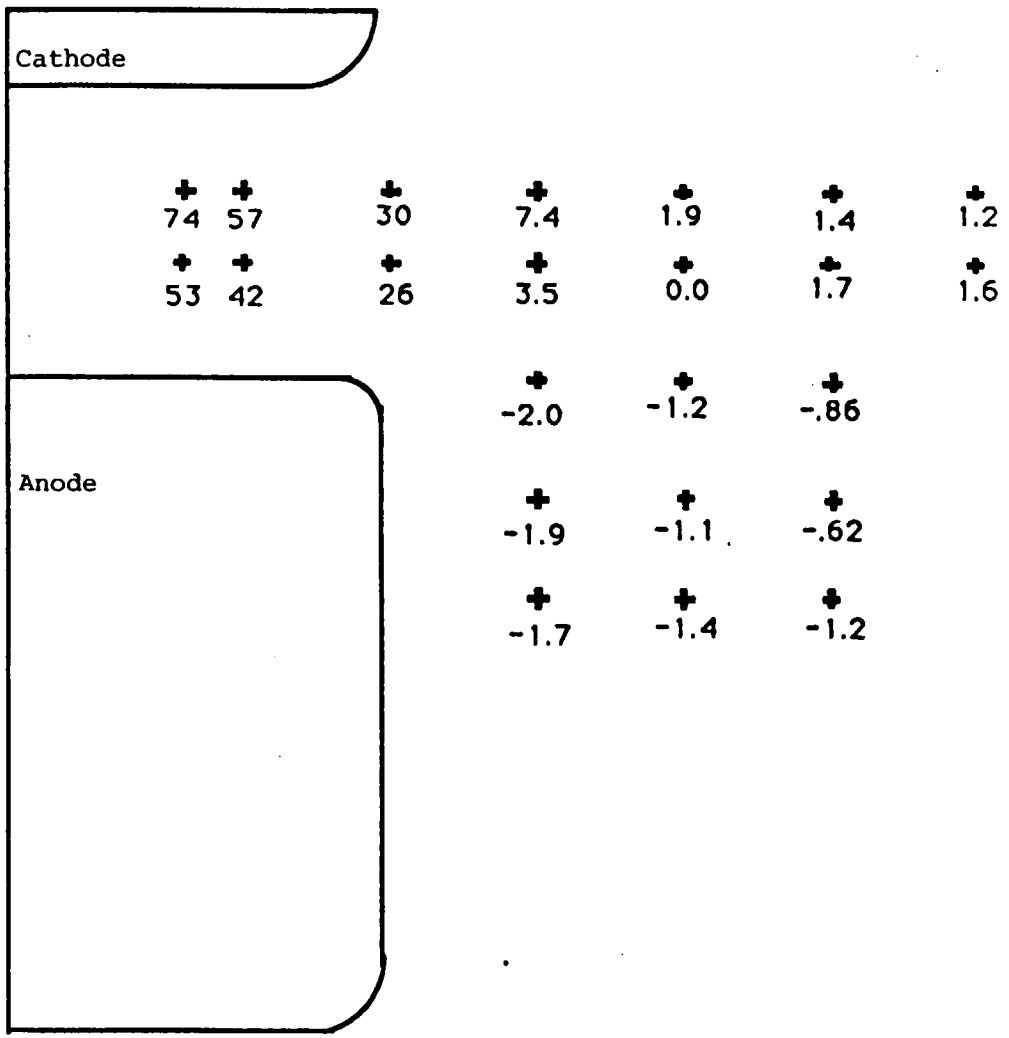

Figure 13: Azimuthal Magnetic Field Data with Applied Magnetic Field (I=2.3kA)

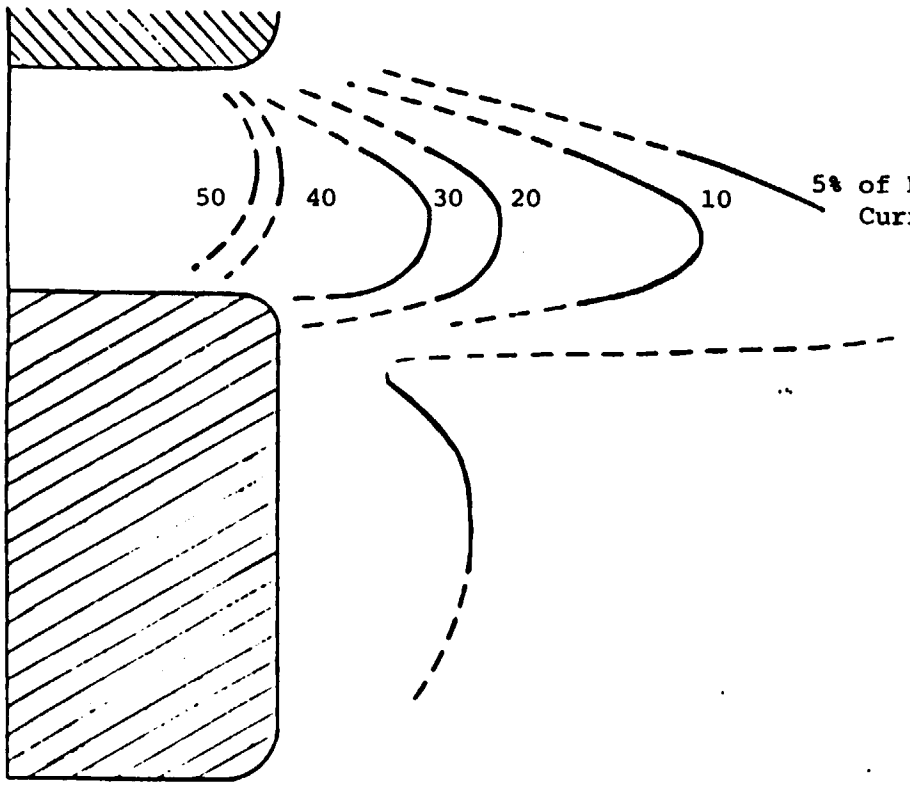

Figure 14: Enclosed Current Profiles without Applied Magnetic Field (I=2.3kA)

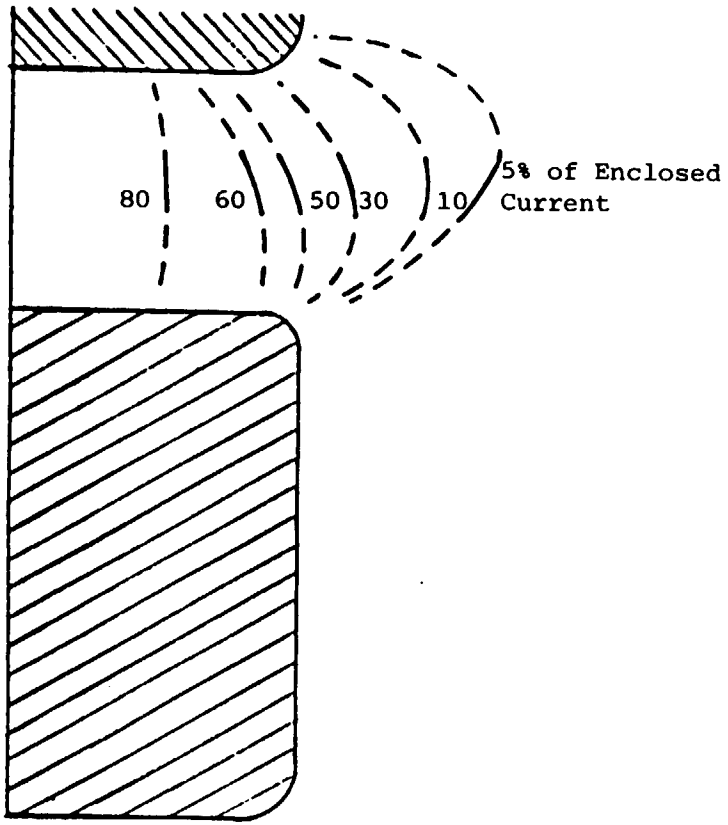

Figure 15: Enclosed Current Profiles with Applied Magnetic Field (I=2.3kA)

by the magnetic pressure induced from the applied magnetic field. Looking at the relative magnitudes of the pressure involved in the experiment, it can be seen that the confinement of the plasma due to magnetic pressure is reasonable. For the nearest axial position at which impact pressure was measured, which will be discussed below, was at z=2 cm. At z=2 cm and r=1 cm the impact pressure, composed of both static and dynamic pressure, was 3.9×10^3 N/m^2 while the magnetic pressure, calculated from $B_z^2/2\mu$, was 3.7×10^3 N/m^2.

4.4 Pressure Profiles

The dramatic effect of the applied magnetic field on the plasma discharge from the thruster be seen in the impact pressure profiles. The impact pressure was measured with the pressure probe described above for power levels of 1.15 kA and 2.3 kA at a mass flow rate of 0.135 g/sec of N_2. The pressure profiles for the 1.15 kA level are shown in Figure 16 and the pressure profiles for the 2.3 kA level are shown in Figure 17. All axial positions are measured from the face of the thruster and all radial positions are measured from the center of the cathode.

The pressure data were taken using single shot operation of the thruster, as was all of the data. The exhaust plume was assumed to be symmetrical and therefore, all of the data that are presented were taken at a fixed azimuthal position. Shots taken at the same radial and axial position but with a 180° difference in azimuthal position agreed with each other to within 10%. The pressure reported for each position is an averaged pressure taken in the flat portion of the pressure record. The initial peak in the impact pressure, which occurs primarily at points within a 2-3 cm radius of the centerline, is believed to be the "blast wave" reported in Reference (6). This, however, has not been

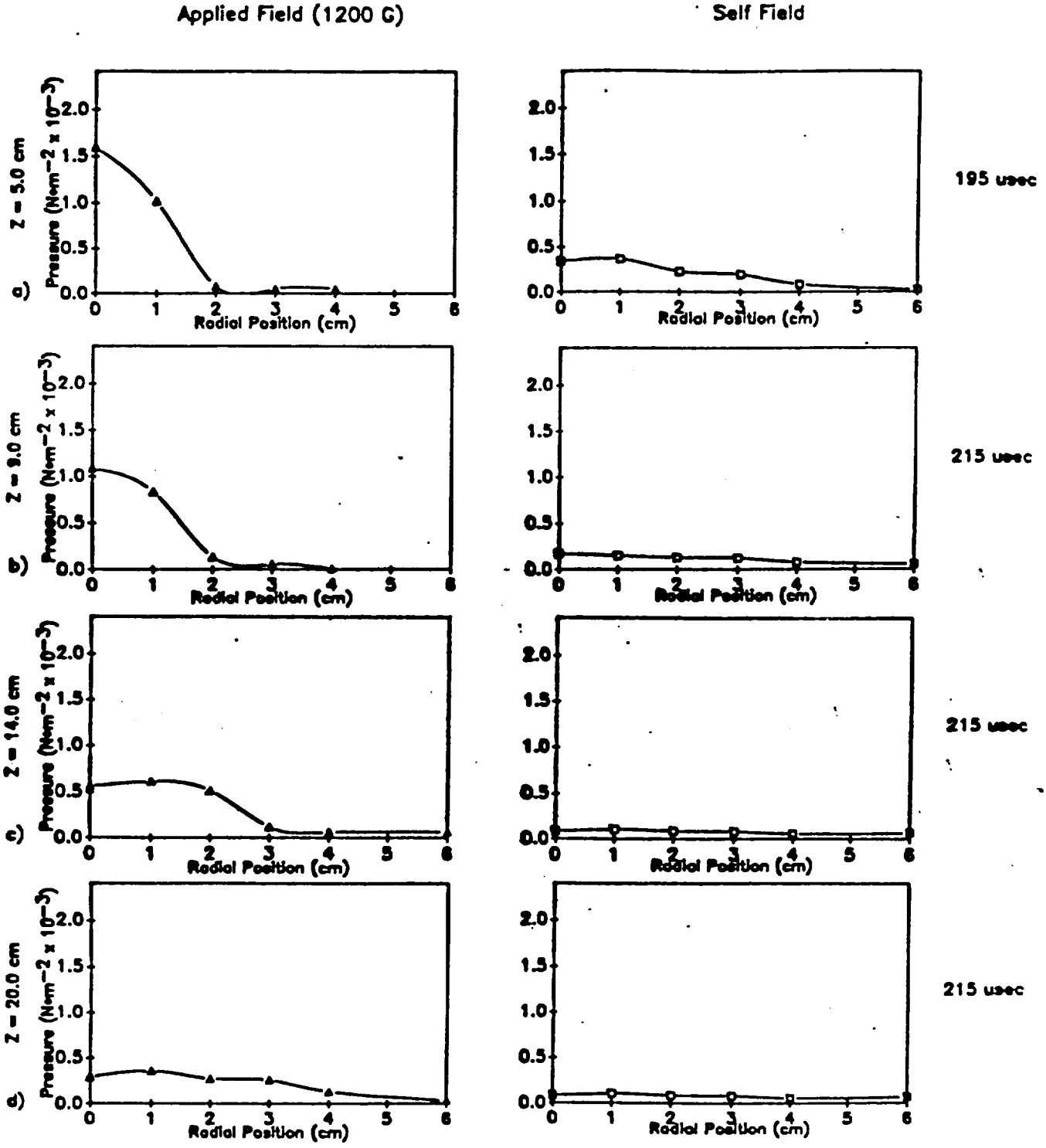

Figure 16: Impact Pressure Profiles for I=1.15kA and $\dot{m}$=0.135gm/sec

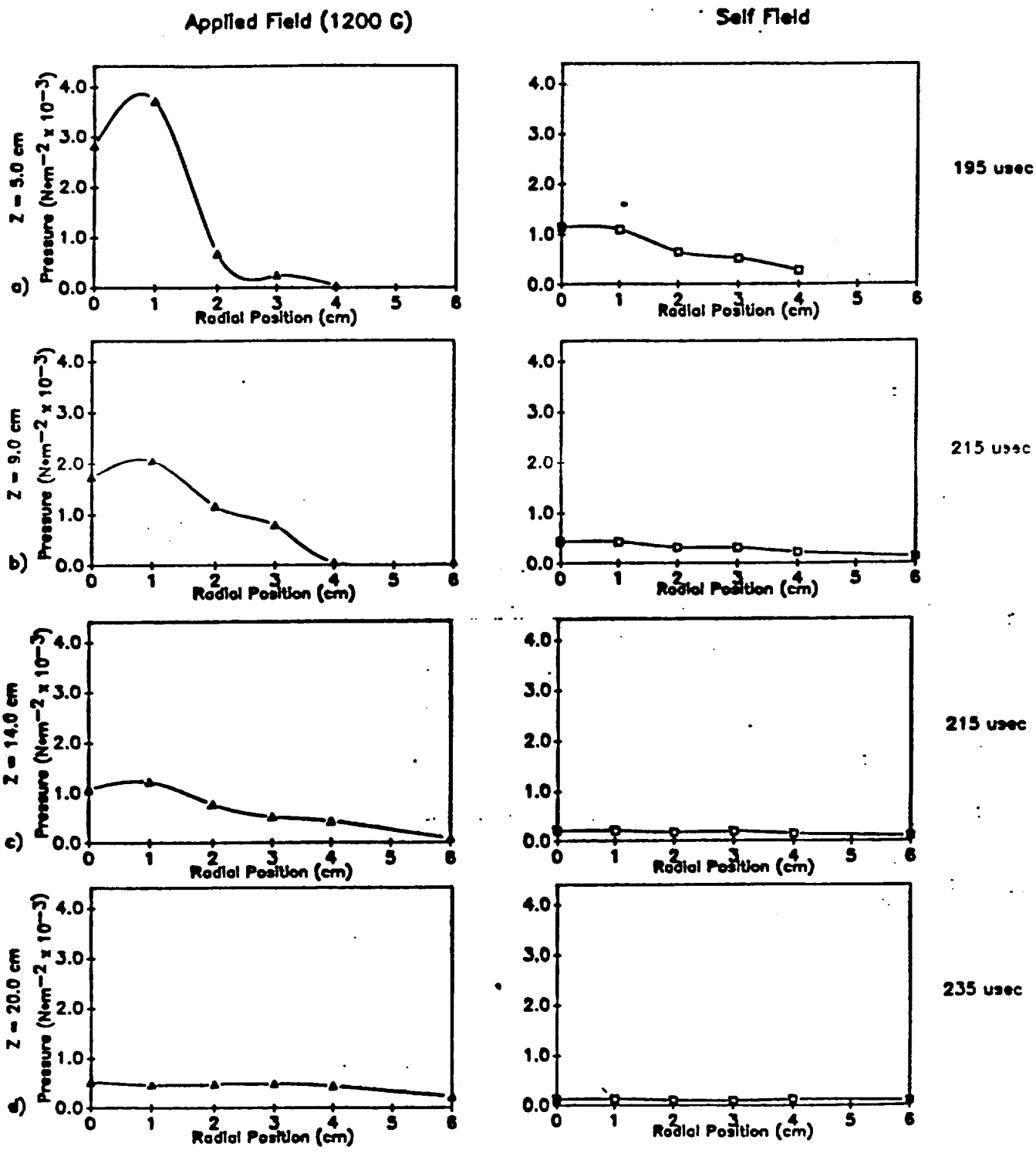

Figure 17: Impact Pressure Profiles for I=2.3kA and $\dot{m}$=0.135gm/sec

investigated. The measured pressure, averaged over ± 20 μsec was taken at a fixed time from the start of the thruster current for each axial stations. The time is noted on the figures and varies between axial positions because of the time the flow requires to move downstream. Pressure variations within the 40 μsec averaging period were typically less than 15%. Shot to shot variation at a specific point was measured by overlaying 5 traces from 5 back to back firings and was found to be within 15%. It should be noted that impact pressure was measured at z=2 cm but is not presented because only the 0 and 1 cm radial positions were valid.

In comparing applied field pressure profiles to self-field ones it can be seen that there is a dramatic increase in impact pressure near the center of the exhaust plume when the applied magnetic is utilized. The results for the 1.15 kA and 2.3 kA current level are very similar, except for absolute magnitudes, and can be discussed together. The only noticeable difference between the 1.15 kA and 2.3 kA power level is the fact that for the applied field case the peak impact pressure occurs at the center for 1.15 kA but occurs near the 1 cm radius for the 2.3 kA level. For both self-field cases the pressure profile at z=5 cm is already spread out over a large portion of the duct with an almost linearly decay moving out in radius. Moving out to z=9 cm the pressure profile for the self field cases is almost entirely flat and remains flat out to the 14 and 20 cm axial positions. For the applied field cases the pressure profile maintains a bell shape out to z=9 cm and the starts to slowly fan out at z=14 cm. Even at 20 cm the applied field pressure profile is not entirely flat. Looking just at the pressure along the centerline it can be seen that the ratio of pressure with the applied field to the pressure without the applied field increases out to z=14 cm. At 5 cm this ratio is approximately 3:1 and at z=14 cm it is about 5.5:1.

These results clearly indicate that the applied magnetic field is compressing the plasma, forcing it to remain in a narrow radius, and allowing a more gradually expansion than a purely self-field case.

From the pressure profiles an indication of thrust and hence specific impulse can be obtained. Assuming the impact pressure is of the form $P_{impact}=(n_c+n_i)\ hT + n_i m_i V^2$, as previously done (7), integration of the impact pressure over the exhaust area will yield the thrust produced by the 1/4-scale MPD. Initial analysis shows that for the self field case thrusts of 1.2 N and 3.0 N for the 1.15 kA and 2.3 kA current levels, respectively, were achieved. For the applied field cases the thrust was increased to 1.9 N for 1.15 kA and to 5.1 N for 2.3 kA. Using the relationship,

$$I_{sp}=\frac{T}{\dot{m}g}$$

the specific impulse's for the various cases were determined. For the 1.15 kA level the self-field case has an I_{SP} of 880 sec while the applied field increases this to 1460 sec. For the 2.3 kA level the self case shows an I_{SP} of 2270 sec while the applied field increase this to 3830 sec. While a more detailed analysis of the thruster operation is needed to determine the physical process responsible for the effects of the applied magnetic field on the 1/4-scale MPD, these results clearly indicate that the applied magnetic field significantly improves the operation of the thruster by increasing thrust and thus specific impulse.

III. DIAGNOSTIC DEVELOPMENT

1. Thomson Scattering Diagnostic For Plasma Flow In Thruster Exhaust

(Emmer)

1.1 Introduction

The Thomson scattering diagnostic is a non-intrusive optical technique used to measure electron density and electron temperature. The principal features, operating characteristics and fundamental theory of the Thomson scattering diagnostic have been discussed in previous progress reports and they will not be repeated here.

1.2 Thomson Scattering Diagnostic: Apparatus, Assembly and System Testing

Assembly of the Thomson scattering diagnostic apparatus has, with minor exceptions, been completed. Overall system testing and check out has begun. Optical components, located in the RFI enclosure (Figure 18), used for focussing, alignment and signal detection, have been installed. Preliminary, operational checks of the transmitting and receiving portion of the optical train have been concluded. Characteristic parameters are listed in Table 3.

Special plexiglas flanges were fabricated to support the Brewster windows. Addition of the flanges improves accessibility into the vacuum vessel and, during required periodic, optical alignment checks, helps to minimize disturbances to other nearby equipment.

Installation of the beam transfer optics has been completed. The transfer optics consist of turning prisms, focussing lenses and assorted apertures that serve two purposes. First, the transmitting optics position and focus the pulsed ruby laser beam to a point inside the vacuum vessel. Second, the receiving

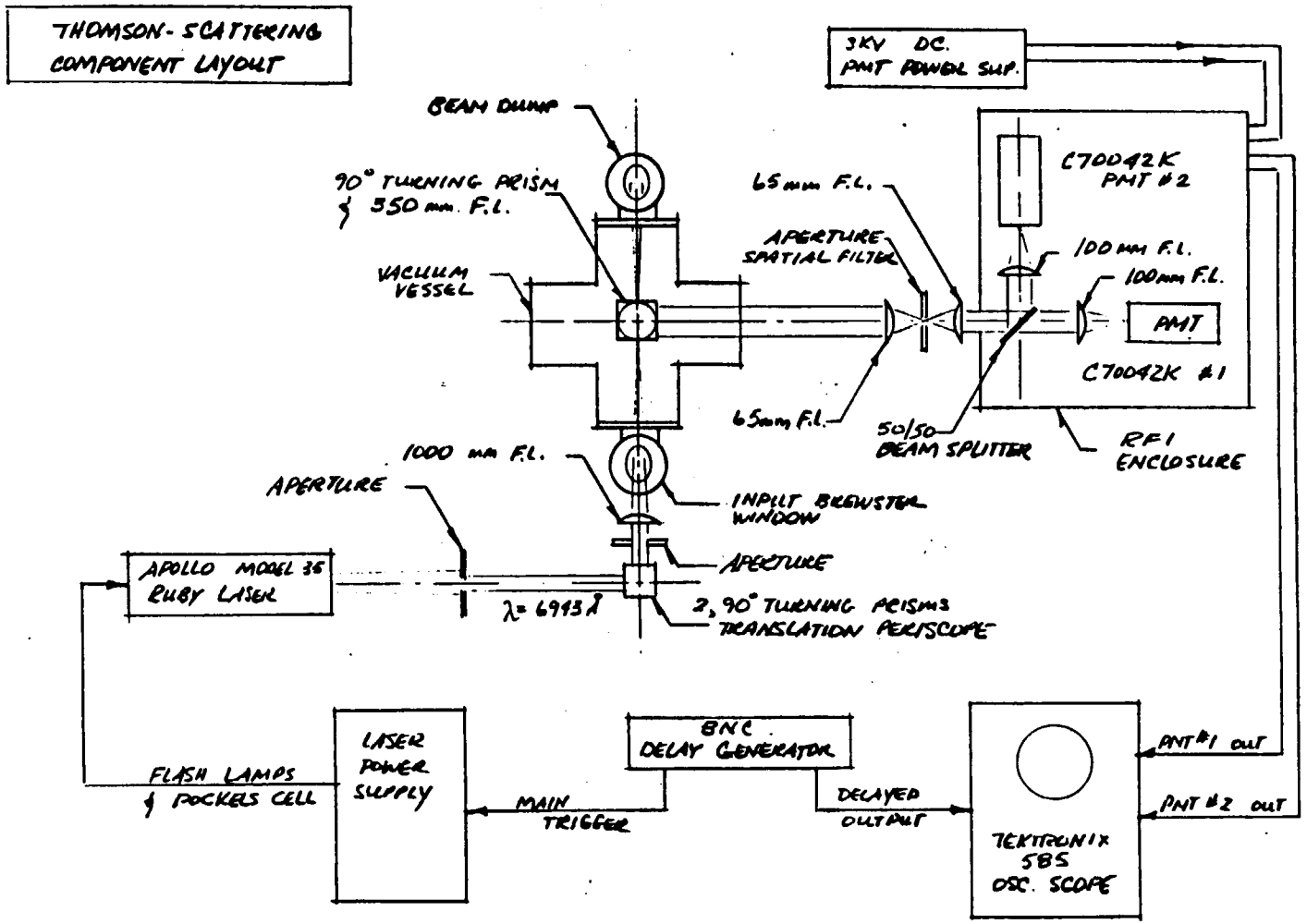

Figure 18: Schematic of Thomson Scattering Layout

Table 3

LASER AND DETECTOR PARAMETERS

I. Laser (Apollo Model 35, Ruby 6943 A)

Energy	3 J
Pulse Length	25 nsec
Beam Diameter	5/8 in.
Scattering Diameter	1.5 mm
Beam Divergence	3.0 mrad

II. Detectors

Type	RCA C70042K
Quantum Efficiency	6% @ 6943 A
Tube Amplification	2×10^5
Number of Photons Gathered	1.30×10^4
Number of Photoelectrons Generated	781
Calculated S/N Ratio of Difference Signal	7

1104.tmy

optics capture and focus the scattered radiation onto the surface of the photomultiplier tubes.

Initial attempts at obtaining oscilloscope recorded, photomultiplier output signals, at 100 Torr pressure levels in the vacuum vessel, were unsuccessful. Several possibilities could explain these results. The most probable cause being the improper synchronization of the time window between the 20 nsec pulse of the laser and the oscilloscope triggering. Alignment errors as well as very low signal levels could also contribute to these observed difficulties.

Alignment checks of the receiving optical train were done using a red LED driven at various frequencies by a Wavetek, frequency generator. The LED was placed inside the vacuum vessel at the ruby laser focal point to simulate the ruby laser intimated radiation source. Results indicated proper alignment and good photomultiplier responses.

Additional system checks are required and the timing issue is currently being investigated.

2. Spectroscopic Techniques and Description of the System

(Mikellides)

2.1 Introduction

Investigation of the radiation emitted from or absorbed by the plasma will be utilized as one of the means of determining its physical properties, such as temperature and particle density. Nitrogen is used as a propellant with ranges of $0.5 < T_e < 2$ eV in electron temperature and $10^{12} < n < 10^{16}/cm^3$ in particle density. Thus, the spectral ranges expected in the exhaust region should be at wavelengths of about 4500 Å and 5500 Å. The smaller wavelengths should represent possible presence of molecular nitrogen in lower current and higher mass flow

tests. Spectral bands of carbon due to contaminants from the materials confining the plasma are also expected.

2.2 Line Broadening Indications of T_e

Doppler broadening of the spectral lines due to random particle motion can be utilized to provide information about the plasma temperature. This is possible since the temperature range expected is low enough to assume a Maxwellian distribution of velocities among the emitting species. The spectral intensity is given by

$$I(\lambda) = \text{constant} \times \exp(-mu^2/kT) \tag{1}$$

and utilization of the Doppler shift ($\nu \simeq c\Delta\lambda/\lambda$) yields

$$I(\lambda) \simeq \text{constant} \times \exp[-mc^2(\Delta\lambda/\lambda)^2/kT] \tag{2}$$

From (1), the width at which the intensity is half the maximum is given by

$$\Delta\lambda_{\frac{1}{2}} \simeq 2.44\times10^{-3}\lambda(T/M)^{\frac{1}{2}} \tag{3}$$

where T is the keV and M is the conventional atomic weight of the emitting species. With the above ranges of T and since M=7, this half-intensity width can be as low as 0.1 Å requiring a spectrograph of high dispersion.

Results from Doppler effect measurements should be confirmed by other types of diagnostics since mass motion and turbulence of the plasma, drift of the ions in a magnetic field and the notion that the velocity distributions are Maxwellian may be sources of error.

2.3 Line Intensity Ratios as Indicators of T_e and N_e

As an alternative method of obtaining the temperature and subsequently particle densities, comparison of line intensities from electronic transitions in a partially ionized gas can be utilized. Specifically, if we assume that the electronic transition responsible for the N line is represented by l→k, and that for the N^+ line by j→i we can write the intensity ratio in terms of the energy difference,

$$\frac{I_{ji}}{I_{lk}} = \frac{\lambda_{ji}A_{ji}g_i}{\lambda_{lk}A_{lk}g_l} \cdot \frac{2(2\pi m_e kT)^{3/2}}{n_e h^3} \exp[-(E_j-E_l)/kT] \qquad (4)$$

where λ is the corresponding frequency of each transition, A the transition probability and g and E are the statistically weight and energy of each corresponding state. All these parameters can be obtained from spectroscopic tabulations so the inverse of the line slope of a linear least-squares fit of the plot

$$\ln\left(\frac{I_{ji}\lambda_{lk}A_{lk}g_l}{I_{lk}\lambda_{ji}A_{ji}g_i}\right) \text{ Vs } (E_l-E_j) \qquad (5)$$

will provide an approximate indication of the temperature in the plasma. This is so since the term $2(2\pi m_e kT)^{3/2}/n_e h^3$ is assumed to be constant for all intents and purposes in the ranges of T and n_e expected.

Once the temperature is obtained, utilization of the Saha equation

$$\frac{n+n_e}{n_o} = \frac{2g^+}{g_o} \frac{(2\pi m_e kT)^{3/2}}{h^3} \exp[-(E^+-E^\circ)/kT] \qquad (6)$$

in conjunction with particle conservation, results in the determination of the electron number density.

2.4 Description of the Spectroscopic System

A Jarrel-Ash Mono-Spec 50 half-meter monochromator will be used since it provides highest stability and maximum resolution of 0.02 Å. As the light enters the entrance slit it is reflected back via a concave mirror and then reflected by a ruled diffraction grating that disperses the light into a series of spectra. The 100 groove/mm grating is blazed at a 6.5 μm wavelength in order to provide a useful spectral range of 4.5 μm - 10.8 μm. The dispersed light is then again reflected and directed through the exit slit towards the photomultipliers.

The optical system, already set up, that will be used in conjunction with the spectrometer consists of a collecting lens placed at a distance of one focal length above the emitting source. Direction of light will then be shifted by 90° by means of a right angle prism and then fed through a double lens that acts as a spatial filter for reduction of noise. As the beam passes through the spectrometer, it then reaches a light tube and finally splits 50-50 by a beam-splitter. Each beam is focused into two photomultipliers and then fed into the oscilloscope for further interpretation of the signal.

IV THEORETICAL MODELLING OF PLASMA FLOW WITHIN MAGNETIC FIELD CONFIGURATIONS (Mikellides)

1. Introduction

As an initial step in the understanding of the fully interactive fields and currents in a MPD arc with applied fields, generation of azimuthal currents by the interaction of the axial motion of charged particles with the magnetic field (Lorentz interaction) will be investigated. In turn, the interaction between the magnetic field and the azimuthal current induces Hall currents which have been shown to be quite influential in highly collisional plasmas.

Specifically, in a pioneer investigation, Okada and Kuriki[8] have included Hall parameters of values much exceeding unity. Both their experimental and theoretical results have shown the rise of a weak charge separation as a consequence of the Hall effect. This induced electric field was found to be stronger in the presence of stronger radial magnetic field gradients. Despite the conclusion of considerable magnitude of such Hall potential, its direct influence on electron density, temperature and velocity distributions has not been determined. The following work initiates that effort.

1.2 Theoretical Background

Electromagnetic interactions are possible when a plasma conducts a current in the presence of a magnetic field. The electromagnetic force acts primarily on the free electrons which carry the current. It is therefore, important to examine the mechanism of momentum exchange from electrons to other particles, as well as the conductivity of the plasma. As we first examine the simple path of a collisionless electron, generation of current is described by Ohm's Law[9]

$$\vec{j} = \sigma[\vec{E} + \vec{V} \times \vec{B}] = \sigma\vec{E}' \qquad (1)$$

where $\vec{E}$ is the electric field, $\vec{V}$ the plasma velocity, $\vec{B}$ the magnetic field and σ the conductivity of the plasma.

Neglecting the thermal motion of the electrons, the path of an electron relative to the gas is a series of curved lines between collisions. The average electron-atom or electron-ion collision, however, results in an electron drift or current which in turn translates to a total loss of electron momentum. This drift motion of velocity $\vec{u}_d$ is shown to contribute to the Lorentz force by means of its cross product with the magnetic field. The resultant force, which is none other than the total draft force, is simply $2\nu_e m_e \vec{u}_d$, and therefore,

$$\vec{E}' + \vec{u}_d \times \vec{B} = \frac{-2\nu_e m_e \vec{u}_d}{e} \simeq \frac{-\nu_e m_e \vec{u}_d}{e} \qquad (2)$$

where ν_e is the average electron collision frequency and the approximation of neglecting the factor of 2 is of no great consequence, since the collision frequency is hardly likely to be known within a factor of 2. Incorporating the current density, $\vec{j}$ and the plasma conductivity, σ into the above equation and then taking the cross product with $\vec{B}$, we can solve for $\vec{j}$:

$$\vec{j} = \frac{\sigma}{1+\omega^2\tau^2}\left[\vec{E}' + \frac{\omega\tau}{B}(\vec{B}\times\vec{E}')\right] = \frac{\sigma}{1+\omega^2\tau^2}\left[\vec{E}+\vec{V}\times\vec{B} + \frac{\omega\tau}{B}\vec{B}_x(\vec{E}+\vec{V}_x\vec{B})\right] \qquad (3)$$

where $\omega = eB/m_e$ is the electron cyclotron frequency and $\tau = 1/\nu_e$ is the average time between electron collisions. The product $\omega\tau$ is the Hall parameter and it has been shown to be greater than unity in certain highly collisional electromagnetic devices. Combining equations (1) and (3), we obtain the generalized Ohm's Law including the Hall effect:

$$\vec{j} = \frac{\sigma}{1+\omega^2\tau^2}\left[\vec{E}+\vec{V}\times\vec{B} - \frac{\omega\tau}{\sigma B}(\vec{j}\times\vec{B})\right] \tag{4}$$

The effect of Hall current, apart from contributing a momentum exchange, is thus a reduction in apparent conductivity by the factor $1/(1+\omega^2\tau^2)^{\frac{1}{2}}$. Considering the plasma a simple resistance, we can see that the effect of the magnetic field is to force the electrons to follow a longer path, in fact, just $(1+\omega^2\tau^2)^{\frac{1}{2}}$ times as long. Thus, the path resistance increases by this factor, or the conductivity decreases by its reciprocal.

Finally, the thermal motion of the electrons is included in equation (4) to produce the following complete expression of current generation due to the Lorentz interaction, Hall effect and thermal motion:

$$\vec{j} = \frac{\sigma}{1+\omega^2\tau^2}\left(\vec{E}+\vec{V}\times\vec{B} + \frac{\omega\tau}{\sigma B}\left[\nabla P_e - \vec{j}\times\vec{B}\right]\right) \tag{5}$$

where $P_e = n_e kT_e$ is the electron thermal pressure.

1.3 Modification of the Theory

The development of the theory[10] utilized six equations and an assumption of a parabolic radial profile for the magnetic field inside the plasma column given by

$$\begin{aligned} B_{zi}(r) &= B_e + (B_e - B_a)(r/a)^2 \quad \text{for } r \le a \\ B_{zi}(r) &= B_e \qquad\qquad\qquad\qquad\quad r > a \end{aligned} \tag{6}$$

where B_e is the applied magnetic field and B_a is the magnetic field at the centerline of the column. The six equations consisted of a continuity equation, two momentum equations; one radial and one axial, two energy equations; one for elec-

trons and one for ions and a magnetic flux equation representing the diffusion of the magnetic field into the plasma. The set is completed by the appropriate boundary and initial conditions. Introduction of the new azimuthal currents developed in the previous section will directly affect two phenomena, namely the $(\vec{j}\times\vec{B})_z$ body force and the Joule heating of the electrons. Consequently, new terms have to be added in two of the above six equations, namely the axial momentum and the electron temperature equations.

The axial momentum equation has been derived using a control volume element analysis. Equation of the net rate of change of momentum inside the volume element to the sum of both body forces and surface forces produced the following expression:

$$\rho\frac{dV}{dt} = \frac{\partial}{\partial z}(P_e+P_i) - \frac{\partial}{\partial z}(\pi_{ai}+\pi_{ae}) + \Pi_{wt}(2\Pi)\frac{r_\nu}{S}\delta_{a,r_\nu} + \frac{1}{S}\int^{s}(\vec{j}\times\vec{B})_z dS' \qquad (7)$$

where

$$\frac{1}{S}\int^{S}(\vec{j}\times\vec{B})_z dS' = 1.411\times10^{5}\frac{B_{re}B_{ze}}{\sqrt{S}}[1-(1-\beta_a)^{\frac{1}{2}}] \qquad (8)$$

and Π_{as} is the s species viscous pressure, π_{wt} is the sidewall ion viscous pressure resulting from contact with the exhaust vessel walls, S is the cross sectional area of the plasma column, $\beta_a=1-(B_a/B_e)^2$ and

$$B_{re} = B_e\mathrm{Sin}[\tan^{-1}(\partial a/\partial z)] \quad , \quad B_{ze} = B_e\mathrm{Cos}[\tan^{-1}(\partial a/\partial z)] \qquad (9)$$

where a is the plasma radius. The reduction of the momentum equation into its final form represented by equations (7) and (8) employed the following assumptions:

(a) The plasma is electrically neutral and consists of only electrons and singly charged ions (hydrogen isotopes) thus, no electric fields are present and interspecies collisional momentum transfer rates add up to zero.

(b) For the device of interest a/L~0.01 where L is the characteristic length of the device, thus

$$\frac{\partial B_r/\partial z}{\partial B_z/\partial r} \sim \frac{a/L}{L/a} \sim \left(\frac{a}{L}\right)^2 \ll 1$$

(c) The radial distribution in plasma, B_r is linear, $B_r(r) \sim B_{re}\, r/a$.

(d) Only diamagnetic azimuthal currents, j_θ are present and flow in a finite thickness sheath.

With the above considerations, we have the following parameters present expressed as vectors in cylindrical coordinates, $\hat{r}$, $\hat{\theta}$, $\hat{z}$,

$$\vec{E} = 0,\ \vec{j} = r j_\theta \hat{\theta},\ \nabla P_e = \partial P_e/\partial z\ \hat{z},\ \vec{V} = V\hat{z} \text{ and } \vec{B} = B_{re}\hat{r} + B_{ze}\hat{z}.$$

Thus, utilizing equation (5) the new azimuthal current to be introduced in terms of plasma resistivity is given by

$$j_\theta = \frac{VB_r \times 10^3}{r\eta_\perp(1+\omega^2\tau^2)c} \tag{10}$$

where $c = 2.9979 \times 10^{10}$ cm/sec is the speed of light. Consequently,

$$(\vec{j}\times\vec{B})_z = -j_\theta B_r \hat{z} = \frac{-VB_r^2 \times 10^6}{r\eta_\perp(1+\omega^2\tau^2)c}\,\hat{z} \tag{11}$$

Finally, integration over the cross sectional area results,

$$\frac{1}{S}\int_S (\vec{j}\times\vec{B})_z dS' = -\frac{0.333\times10^{-4}V}{\eta_\perp(1+\omega^2\tau^2)S}\, 2\Pi_o^a \int B_{re}^2 \frac{r^2}{a^2}\, dr = \frac{-0.699\times10^{-4}VB_{re}^2 a}{\eta_\perp(1+\omega^2\tau^2)S} \tag{12}$$

where all the parameters are in cgs units except the magnetic field which is expressed in KG. Thus, the updated momentum equation becomes

$$\rho\frac{dV}{dt} = \frac{\partial}{\partial z}(P_e+P_i) - \frac{\partial}{\partial z}(\Pi_{ai}+\Pi_{ae}) + \Pi_{wi}\,(2\Pi)\,\frac{t_r}{S}\,\delta_{a,r},\, +$$

$$+ 1.411\times10^5 \frac{B_{re}B_{ze}}{\sqrt{S^1}}[1-(1-\beta a)^{\frac{1}{2}}] - \frac{0.394\times10^{-4}VB_{re}^2}{\eta_\perp(1+\omega^2\tau^2)\sqrt{S}} \tag{13}$$

Equation of the time rate of change in plasma energy, consisting of both thermal energy and kinetic energy, plus the net flux of plasma energy into the control volume element with the sum of the net rate of work done on that element due to surface forces and the net heat flux into the volume due to thermal conduction, resulted in the following expression, referred to as the electron temperature equation,

$$\frac{d}{dt}(kT_e) = (\gamma-1)kT_e\frac{1}{n}\frac{dn}{dt} + \frac{(\gamma-1)}{nS}\frac{\partial}{\partial z}\left(K_e S\frac{\partial T_e}{\partial z}\right) + \frac{k(T_i-T_e)}{\tau}$$

$$- \frac{(\gamma-1)}{nS}\Pi_{ae}\frac{\partial VS}{\partial z} + \frac{(\gamma-1)}{nS}P_j - \frac{2(\gamma-1)}{nr_v}q_{we}\,\delta_{a,r}, \tag{14}$$

where T_e is the electron temperature, n the number density, K_e the thermal conductivity, q_{we}, the flux of electron heat from the plasma across the magnetic field lines into the exhaust-vessel sidewalls and P_j is the ohmic heating which arises from thermalization of electron diamagnetic currents,

$$P_j = \int_S \eta_\perp j_\theta^2 dS' = 2.235\times10^{34}B_e^2\eta_\perp[1-(1-\beta a)^{\frac{1}{2}}] \tag{15}$$

Obviously, the ohmic heating of electrons will increase with the introduction of the azimuthal currents due to Lorentz interaction and Hall effect. Specifically, from equation (10),

$$j_\theta^2 = \left[\frac{VB_r x10^3}{r\eta_\perp(1+\omega^2\tau^2)C}\right]^2 = \frac{1.113x10^{-15}V^2B_r^2}{r^2\eta_\perp^2(1+\omega^2\tau^2)^2} \tag{16}$$

and thus, integration over the cross sectional area yields

$$P_j = \int_S \eta_\perp j_\theta^2 dS' = \int_0^a \eta_\perp \frac{1.113x10^{-15}V^2B_{r_e}^2\, r^2/a^2}{r^2\eta_\perp^2(1+\omega^2\tau^2)^2} 2\pi r dr =$$

$$= \frac{1.113x10^{-15}V^2B_{r_e}^2 \cdot 2\pi}{\eta_\perp(1+\omega^2\tau^2)^2a^2} \int_0^a r dr = \frac{3.497x10^{-15}V^2B_{r_e}^2}{\eta_\perp(1+\omega^2\tau^2)^2} \tag{17}$$

Thus, the updated term for the Ohmic heating, P_j, that will be inserted in the electron temperature equation, (14) becomes

$$P_j = 2.235x10^{34}B_e^2\eta_\perp[1-(1-\beta a)^{\frac{1}{2}}] + \frac{3.497x10^{-15}V^2B_{r_e}^2}{\eta_\perp(1+\omega^2\tau^2)^2} \tag{18}$$

1.4 Summary and Conclusions

The generation of azimuthal currents due to Lorentz interactions and the Hall effect have been introduced to the set of equations that simulates plasma flow confined by a magnetic field. This was achieved by utilizing the generalized Ohm's law and then deriving the terms resulting from the Hall current. From the updated momentum and electron energy equations, we note that a loss of total momentum, and consequently retardation of the flow, and an increase in the rate of change of electron temperature should be expected.

Future goals include the proper differencing of the new terms and then insertion into the computer code. Further objectives should include the generation of radial and axial currents and consequently an induced azimuthal magnetic field.

V. MULTIBEAM INTERFEROMETRY WITH CO_2 LASER

COMPLIMENTARY RESEARCH STUDIES (AFOSR)
(Kiritsis)

1.1 Interferometry - Theory

One of the major parameters to be measured during a plasma discharge is the radially dependent electron density $N_e(r)$. Interferometry is used to measure quantities from which information can be extracted about $N_e(r)$.

When an electromagnetic wave propagates in a plasma discharge it undergoes a phase shift which is given by:

$$\phi = 2.82\ 10^{-13}\ \lambda_o \int_{z_1}^{z_2} N_e(z)dz$$

where ϕ = the phase shift

λ_o = the wavelength of the radiation

$N_e(z)$ = the chord dependent electron density

According to the formula above, the phase shift is proportional to the wavelength of the radiation used and the chord averaged electron density. Using simple interferometry ϕ can be measured but the measurement is inaccurate due to the fact that the signal obtained is only proportional to the cosine of ϕ. Thus, it is impossible to determine if ϕ is increasing or decreasing. In addition to that, variations in the product of the scene beam with the reference beam can be wrongly interpreted as changes in ϕ. To overcome these difficulties phase modulation should be used. The technique involves the following: the signal through one leg of the interferometer is first shifted up in frequency, then as it propagates through the plasma is phase modulated by an angle ϕ and eventually the frequency shifted, phase modulated signal combines with the original source signal. The combined beam is detected by a detector and the detector output

enters a comparator where it gets compared to the modulation frequency. The comparator outputs two signals, one proportional to the cosine of the phase shift ϕ and the other is proportional to the sine of ϕ and thus, unambiguous calculation of the phase shift ϕ can be made. Knowing ϕ, the chord-averaged electron density can be calculated. In order to calculate the radially dependent electron density a transformation must be applied on to the chord-averaged electron density. This transformation requires information about the chord-averaged electron density in several locations in the plasma and simple one channel interferometry is not able to provide that information. Thus, multi-beam interferometry should be used with more than one channels.

Since the phase shift ϕ is directly proportional to the wavelength of the radiation used as shown by the formula above, longer wavelengths will produce larger ϕ values thus making the phase shift easier to detect. During the first stage of this study, CO_2 laser radiation at 10.6 microns will be used for electron density measurements. In the future, FIR radiation (methyl alcohol laser at 118.9 microns) can be considered for the same electron density measurements.

1.2 Interferometry - Experiment

The optical scheme of the proposed multi-beam interferometer is shown in Figure 19. The experiment was initially designed with 5 independent channels but due to limited funds it will be assembled with only 4 channels at the present. When money becomes available in the future, the 5th channel will be added.

The output of the CO_2 laser (Apollo Laser Inc., Model 570) is down collimated from an 8mm diameter to a 5mm diameter and then it enters the germanium acousto-optic cell (Intra-Action Corp., Model AGM-406B). The acousto-optic modulator operates as a frequency shifter. It splits the input beam into two output

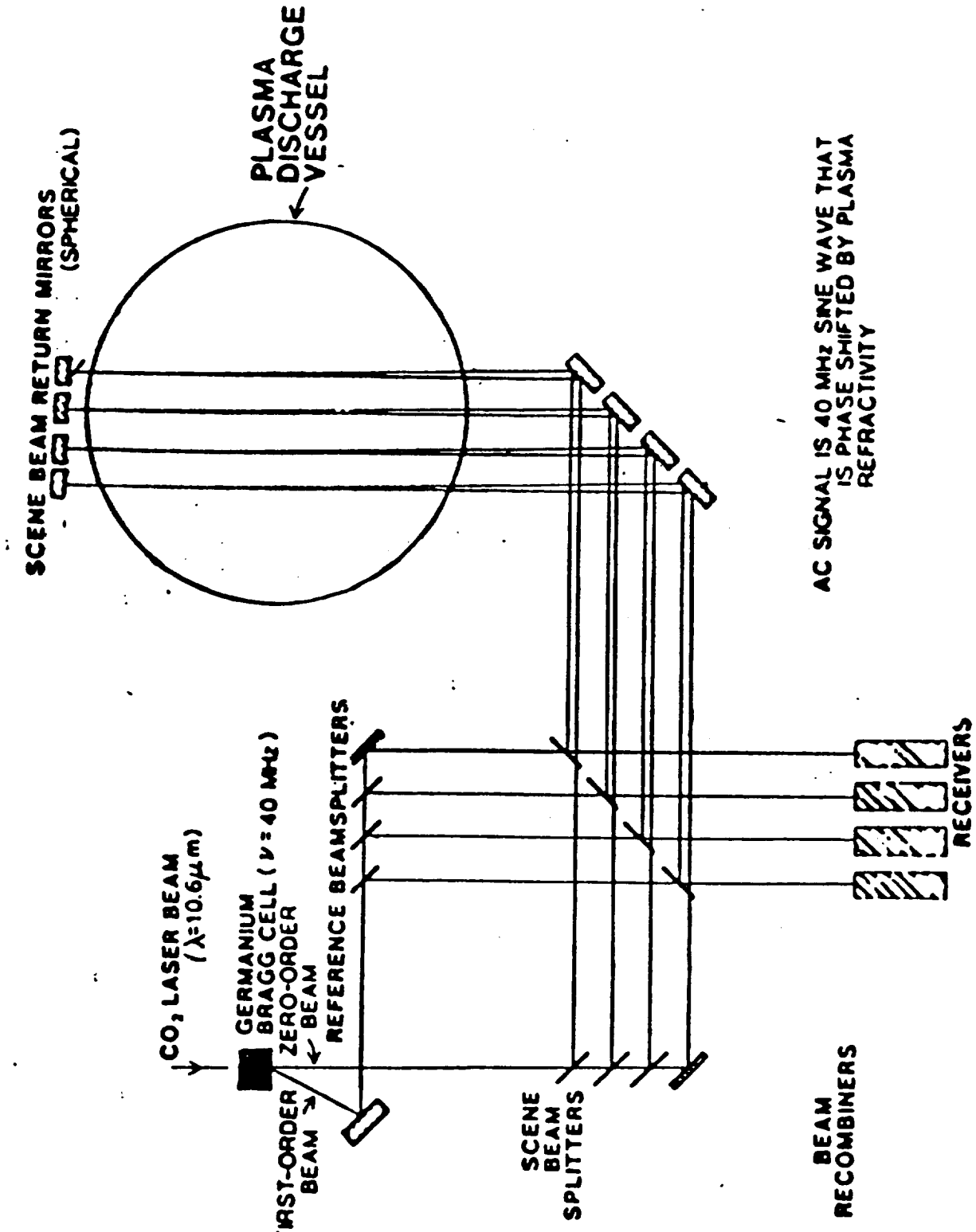

Figure 19: Schematic of Multi-Beam Interferometer

beams, the scene beam (zero-order) and the reference beam (first-order), and shifts the frequency of the reference beam up by 40MHz with respect to the frequency of the scene beam. The first order beam illuminates the four reference paths of the interferometer and the zero order beam illuminates the four scene paths. The intensity of each one of the reference and scene beams is kept at about 20%. The paths of the scene beams are as follows: through the scene beam-splitters, to the reflecting flat mirrors, through the plasma to the reflecting concave mirrors, through the plasma for the second time to the flat mirrors again and finally onto the beam recombiners. The beam recombiners combine the reference beams as they come from the source with the scene beams as they come from the plasma and then the combined output beams are focused onto the detectors.

The power detected by the detectors contains an oscillating component at 40MHz due to the interference between the reference and the corresponding scene beams, and it is also phase modulated due to the propagation of the scene beams through the plasma. All four receivers are the same. When the radiation is detected by the thermoelectrically cooled detectors (Electro-optical Systems Inc., Model MCT10-T1-002) a signal proportional to the input power is generated. The signal is amplified by a first stage amplifier and an amplifier and then enters the quadrature phase detector (Merrimac Industries Inc., Model PCM-3-40B). The phase detector generates two signals, one is proportional to the cosine of the phase shift due to the plasma and the other is proportional to the sine of the phase shift. The major advantage of this technique is that the phase shift can now be calculated unambiguously. A function generator set at 40MHz drives each one of the four quadrature phase detectors and the acousto-optic cell. An eight channel waveform recorder (Gould Electronics, Model 4386) will be used to digitize and store all the sine and cosine signals while the experiment is in

progress. The stored data will then be transferred through a IEEE-488 bus (Metrabyte, Model IE-488) to a PC (DELL Computer Corp., System 316SX) for further analysis. The commercially available scientific software ASYST 3.0 will be used for analysis and graphing/presentation purposes.

1.3 Preliminary Investigation of the Beam "Quality"

Before using the CO_2 laser system for the proposed experiment some external beam parameters will have to be measured. It is important that these parameters are known before the radiation is used for the experiment because the obtained results will depend on them. The parameters that will be measured are as follows.

1.3.1 Intensity Profile of the Beam, Beam Size

The beam's intensity pattern versus the distance across the beam (intensity profile) is of a great importance. The intensity profile will be measured in both X and Y directions as shown in Figure 20, for both, the near field portion of the beam and the far field portion of it. Knowing the intensity profile of the beam allows the determination of the beam size. The beam size is defined as the diameter of the beam that contains a usable percentage of the total beam energy. This diameter can be defined between positions where the intensity has fallen to the user selected, 1/e, 1/e2, FWHM values with respect to the beam's peak intensity level. Figure 21 depicts that information.

The intensity profile will be measured by scanning a detector sensitive to CO_2 radiation wavelength (10.6 microns) across the beam's diameter and recording the power incident on the detector. The detector will be set on a motorized stage which will move across the beam with a predetermined constant speed. The

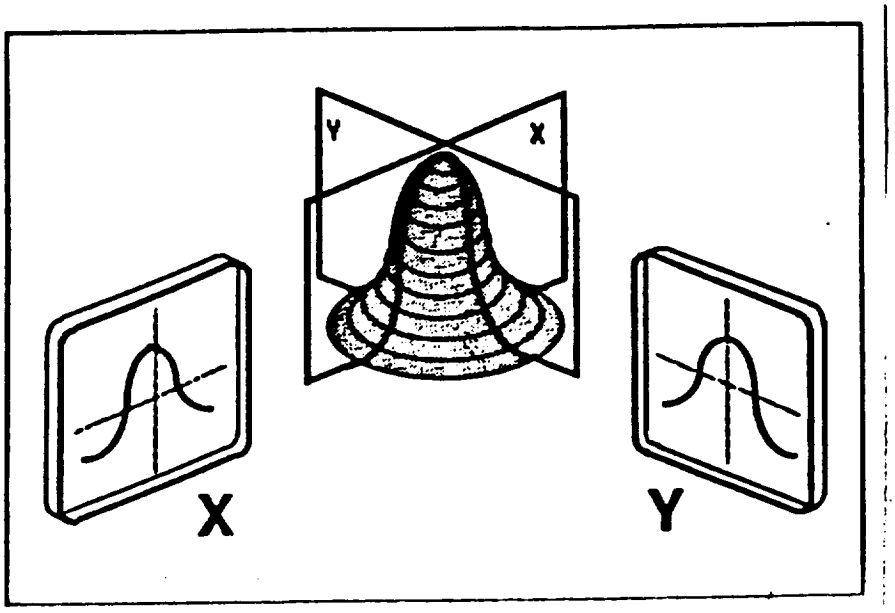

Figure 20: Intensity Measurements Made in X and Y Planes

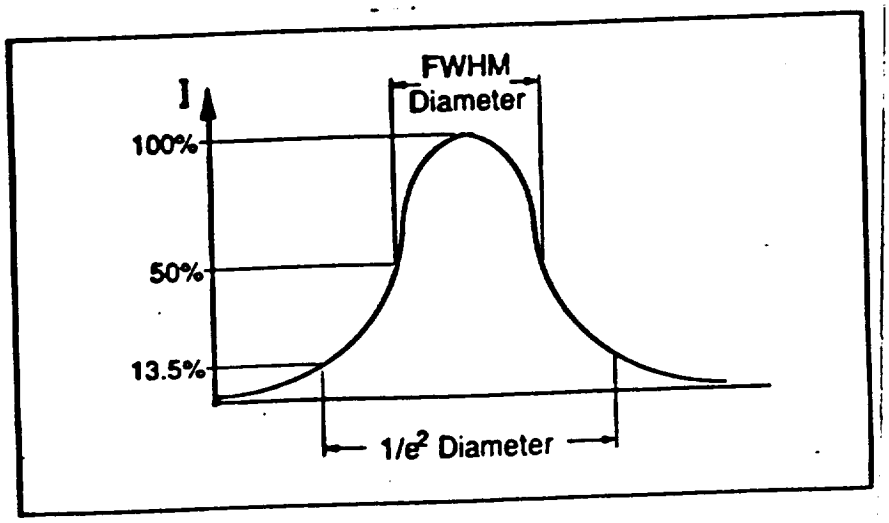

Figure 21: Definition of Beam Intensity Parameters

detected power will be digitized and stored in the waveform recorder mentioned above for further analysis and plotting. In order to measure the intensity profile in the other direction, the motorized stage with the detector will be mounted in a 90 degree angle with respect to the latter position. Displaying the intensity profile on a monitor will determine weather the intensity distribution is the appropriate or not.

1.3.2 Beam Divergence

Another quantity which is desirable to be known is the degree of collimation of the beam. Most beams change in size as they propagate, and the rate in which the beam grows is known as the divergence. This angular measure of the beam can be determined by knowing the intensity profile. First, two beam diameters d1 and d2 will be measured at two different locations in the beam path, l1 and l2 respectively. Then the difference between the measured beam diameters divided by the distance between the points of measure will give the divergence angle. Implementing the above statement in an equation results in:

$$\text{Divergence angle} = \frac{d2 - d1}{l2 - l1}$$

The requirement that l1 > (d**2/wavelength) has also to be filled when the divergence is measured as stated above. Figure 22 is a sketch of the actual situation.

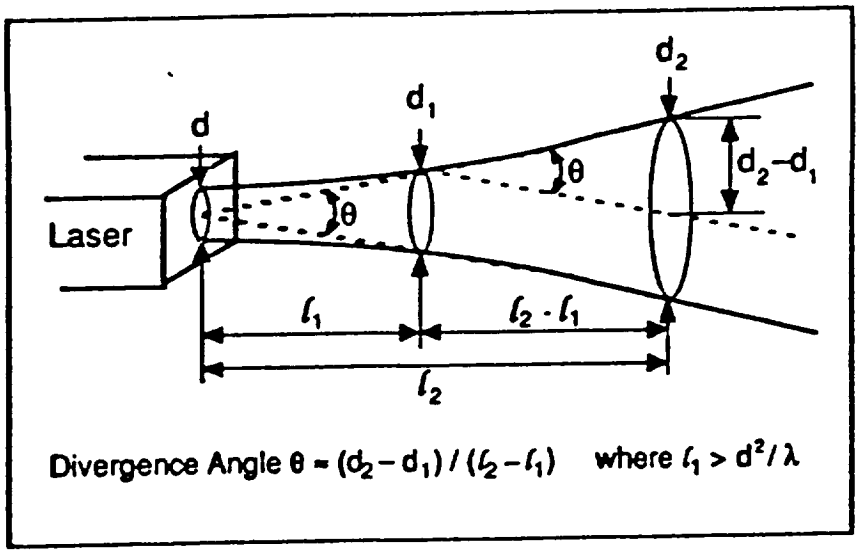

Figure 22: Determination of Beam Divergence Parameters

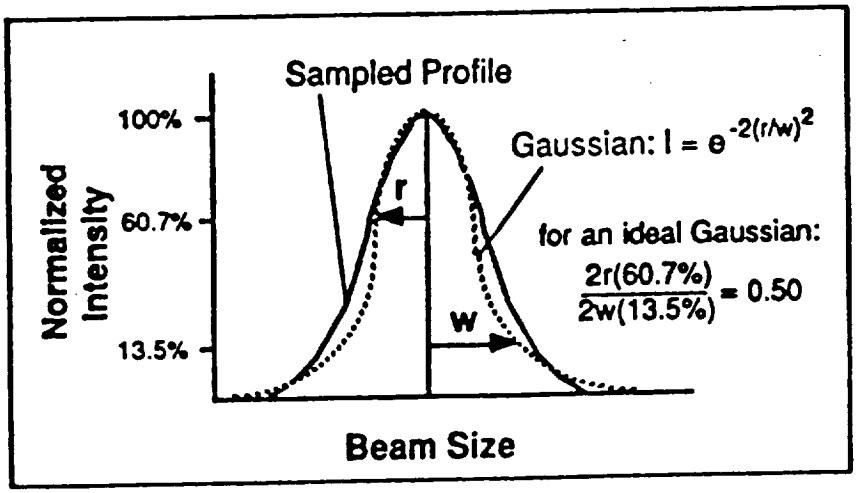

Figure 23: Identification of Beam Radiation Patterns

1.3.3 Laser Stability

Stability is a characteristic of both the frequency that a laser operates in and the output that it produces. For Apollo Laser's Model 570 frequency stability is immediate after changing the tuning to a different wavelength.

On the other hand, the output power delivered by the laser is not stable for the first 2 meters of the beam path (telephone conversation with the manufacturer). In order to investigate this, the average power delivered will be measured by a power meter for a fairly long period of time while the data taken are digitized and stored. The analysis of the data will involve calculations of the mean power, percent change in power, standard deviation for all the samples taken and depending on the results the stability of the laser will be determined.

1.3.4 Percent of a Gaussian Beam in the Output Beam

The radiation pattern of a laser is closely linked to the characteristics of the laser resonator. Transverse modes refer to the patterns of light across the beam as they emerge directly from the laser. Apollo's Model 570 will be operated in the TEM00 mode. A TEM00 mode has a smooth gaussian profile while other higher order modes tend to cause the beam to spread out. The percentage of Gaussian beam within a mixed mode beam can be determined by comparing the diameters at two intensity levels as shown in Figure 23.

VI. Faculty and Staff Participation

T.M. York	Principal Investigator	
	July 1, 1989 - Dec. 31, 1989	0%
D.S. Emmer	Research Associate	
	July 1, 1989 - Oct. 31, 1989	10%
P. Mikellides	Graduate Research Associate	
	Aug. 1, 1989 - Sept. 15, 1989	50%
	Sept. 15, 1989 - Dec. 31, 1989	25%
G. Soulas	Graduate Research Associate	
	July 1, 1989 - Dec. 31, 1989	50%
C. Zakrzwski	Graduate Research Associate	
	July 1, 1989 - Sept. 15, 1989	50%

VII. REFERENCES

1. York, T.M., Semi-Annual Progress Report for the Period January 1, 1988 to June 30, 1989, AAE Report AARL-P-89-2, August 1, 1989.

2. Cobine, T.D., Gaseous Conductors, Dover Publications, Inc., New York, 1958.

3. Kaplan, D.J., "Performance Characteristics of Geometrically Scaled MPD Thrusters," M.S.E. Thesis, Princeton University, Princeton, NJ, February 1982.

4. Sovey, J.S. and Mantenieks, M.A., "Performance and Lifetime Assessment of MPD Arc Thruster Technology," AIAA Paper 88-3211, AIAA 24th Joint Propulsion Conference, Boston, MA, July 11-13,1988.

5. Mims, F.M., Engineer's Mini-Notebook: Op Amp IC Circuits, Siliconcepts, United States, 1987.

6. Michels, C.J. and York, T.M., "Pressure Measurements in the Exhaust of a Pulsed Megawatt MPD Arc Thruster," AIAA Paper 71-196, January 1971.

7. Michels, C.J. and York, T.M., "Exhaust Flow and Propulsion Characteristics of a Pulsed MPD Arc Thruster," AIAA Paper 72-500, April 1972.

8. Okada, O. and Kuriki, K., "The Interaction Between a Plasma Flow and a Magnetic Nozzle with Strong Hall Effect," Int. of Space & Aero. Sci., U. Tokyo Rept. 457, Dec 1970.

9. York, T.M., "AIAA Electric Propulsion Short Course," July 8-9, 1989, Monterey, CA, Electromagnetic Propulsion.

10. Stover, E.K., "Computer Simulation of Plasma Behavior in Open-ended Linear Theta Machines," (Ph.D. Thesis, Penn State University) DOE Report ET-53018-6, April 1981.